PHYSICAL REVIEW B **85**, 075118 (2012)

Coherent control of correlated nanodevices: A hybrid time-dependent numerical renormalization-group approach to periodic switching

Eitan Eidelstein and Avraham Schiller
Racah Institute of Physics, The Hebrew University, Jerusalem 91904, Israel

Fabian Güttge and Frithjof B. Anders
Lehrstuhl für Theoretische Physik II, Technische Universität Dortmund, DE-44221 Dortmund, Germany
(Received 18 November 2011; revised manuscript received 15 January 2012; published 15 February 2012)

The time-dependent numerical renormalization-group approach (TD-NRG), originally devised for tracking the real-time dynamics of quantum-impurity systems following a single quantum quench, is extended to multiple switching events. This generalization of the TD-NRG encompasses the possibility of periodic switching, allowing for coherent control of strongly correlated systems by an external time-dependent field. To this end, we have embedded the TD-NRG in a hybrid framework that combines the outstanding capabilities of the numerical renormalization group to systematically construct the effective low-energy Hamiltonian of the system with the prowess of complementary approaches for calculating the real-time dynamics derived from this Hamiltonian. We demonstrate the power of our approach by hybridizing the TD-NRG with the Chebyshev expansion technique in order to investigate periodic switching in the interacting resonant-level model. Although the interacting model shares the same low-energy fixed point as its noninteracting counterpart, we surprisingly find the gradual emergence of damped oscillations as the interaction strength is increased. Focusing on a single quantum quench and using a strong-coupling analysis, we reveal the origin of these interaction-induced oscillations and provide an analytical estimate for their frequency. The latter agrees well with the numerical results.

DOI: 10.1103/PhysRevB.85.075118 PACS number(s): 03.65.Yz, 73.21.La, 73.63.Kv, 76.20.+q

I. INTRODUCTION

The quantitative description of real-time dynamics in strongly correlated systems is one of the outstanding challenges of contemporary condensed-matter physics, with relevance to varied systems ranging from cold atoms[1,2] and dissipative systems[3] to quantum-dot devices[4,5] and biological donor-acceptor molecules.[6] Alongside fundamental questions concerning the underlying time scales and the long-time behavior, there are many technological issues that require careful investigation. For example, the decoherence and relaxation of spins appears to be the major obstacle for the realization of quantum-computing algorithms in real systems.[7] Another key issue is the understanding of coherent control and the switching characteristics of nanodevices such as single-electron transistors.[8] These and related topics require the development and application of suitable many-body techniques.[9]

Over the years, the Kadanoff-Baym[10] and Keldysh[11] techniques have proven to be accurate tools for describing the real-time dynamics of weakly correlated systems such as light-matter interaction in semiconductors[12] and the decoherence and relaxation of an impurity spin well above the Kondo temperature.[13] Geared toward perturbation theory, these techniques generally fail upon the development of strong correlations, when nonperturbative approaches are in order. A case in point are quantum dots tuned to the Kondo regime,[14] where traditional diagrammatic-based approximations are unsuitable to describe the nonequilibrium state.[15] The difficulty lies in the fact that strongly correlated systems change their nature as a function of certain control parameters such as the temperature or the coupling constants, an aspect well captured by renormalization-group approaches.[16,17] The precise status of a voltage bias as yet another control parameter in interacting nanostructures is still under debate.

Recent years have witnessed an impressive advancement of numerical techniques aimed at tracking the real-time dynamics of strongly correlated systems, primarily with the development of the time-dependent density-matrix renormalization group (TD-DMRG).[18–21] Yet while the adaptive TD-DMRG works remarkably well on time scales of order the reciprocal bandwidth, it is presently unsuited for tackling longer time scales due to an accumulated error that grows first linearly and then exponentially with the time elapsed. Alternative formulations[22] of the TD-DMRG circumvent the accumulated error, but are simply too demanding to advance to long times. Recent adaptations of continuous-time Monte Carlo techniques to real-time dynamics[23–26] are free of finite-size effects, but are confined to short time scales due to an inherent sign problem. The Chebyshev expansion technique,[27] developed by Tal Ezer and Kosloff,[28,29] offers yet another extremely powerful approach for tracking the time evolution of finite-size systems. However, it too is quite limited in accessing long time scales in the presence of interactions due to the exceedingly large Hilbert space that must be retained. A complementary approach is provided by the time-dependent numerical renormalization group (TD-NRG).[30–32] The TD-NRG can successfully bridge over vastly different time scales, but is far more restrictive in the systems and perturbations to which it can be applied. A composite approach that combines the complementary traits of the different techniques mentioned above is highly desirable.

In this paper, we devise such a hybrid approach that combines the outstanding capabilities of the numerical renormalization group (NRG) to systematically construct the effective low-energy Hamiltonian of the system[16,33] with the prowess

of complementary approaches for calculating the real-time dynamics derived from this Hamiltonian. Typically strongly correlated systems possess multiple energy scales that markedly differ in magnitude, hence their dynamics is governed by vastly different time scales. This spread of time scales, which may differ by many orders of magnitude, poses an enormous obstacle for most computational approaches. The TD-NRG is quite unique in this respect as it can efficiently bridge between the different time scales. Our hybrid approach presented below provides a flexible platform for combining the TD-NRG with one's method of choice for treating the effective low-energy Hamiltonian. Possible choices for the complementary method could be exact diagonalization, the TD-DMRG, and possibly also the time-dependent noncrossing approximation.[34,35] Here we shall demonstrate the applicability of our approach by combining the TD-NRG with the Chebyshev expansion technique (CET), providing thereby an important proof of principle.

The basic philosophy underlying the hybrid-NRG is to first exhaust the TD-NRG in order to decompose the time-dependent wave function into distinct components, each associated with a separate time scale and evolving according to its own reduced Hamiltonian acting on a suitable subspace of the full Fock space. Each of the individual components with its associated Hamiltonian can then be treated with improved accuracy using, e.g., the TD-DMRG or CET. In this manner, one can exploit the successive reduction in energy scales in order to boost the TD-DMRG and CET to long time scales that otherwise would be inaccessible to either of these methods. Concomitantly, the accuracy and flexibility of the TD-NRG are greatly enhanced, as we demonstrate by extending the approach to the physically relevant case of repeated switchings. The hybrid platform further offers an appealing way to reduce discretization errors inherent to the Wilson chain by converting to hybrid chains.

The idea to use the NRG level flow to construct effective Hamiltonians is, of course, not new. Dating back to the original work of Wilson,[16] this framework has been significantly advanced by Hewson[33] who used it as a starting point for devising a renormalized perturbation theory. Hewson's approach requires, however, analytical knowledge of the form of the low-energy Hamiltonian and its associated quantum field theory. So far, it has been applied mainly to the single-impurity Anderson model, where it was used, among other things, to calculate the steady-state current [33,36] in the limit of a small bias voltage.

Our approach is far more general as it makes no assumption on the analytical form of the effective Hamiltonian. Rather, it is solemnly based on Wilson's original concept[16] that the NRG level flow contains all accessible information, and, in particular, can accurately describe the crossover region between two distinct fixed points (a regime that generally lies outside the reach of perturbative methods). Our framework exclusively uses the sequence of diagonalized NRG Hamiltonians,[16] circumventing thereby any prejudice on the form of the effective Hamiltonian. As a result, our method is model independent, relying solely on the NRG approach itself.

In this paper, we extend the original TD-NRG algorithm from a single quantum quench to multiple switchings, which requires an additional approximation beyond the one underlying the conventional TD-NRG. As we demonstrate by explicit calculations, the quality of the approximation can be systematically improved by enlarging the subspace treated using the complementary method.

A. Preliminaries

In the TD-NRG, the continuous bath is represented by a discretized Wilson chain,[16] characterized by tight-binding hopping matrix elements that decay exponentially along the chain. This separation of energy scales enables access to exponentially long time scales[30,31] that otherwise would be inaccessible using ordinary tight-binding chains. In analyzing the accuracy of the TD-NRG, it is important to distinguish between two sources of error: one extrinsic due to the discretized representation of the continuous bath in terms of a Wilson chain, and the other intrinsic due to the TD-NRG algorithm for tracking the real-time dynamics on the Wilson chain.

As already noted in Ref. 31, the latter source of error is remarkably small. We illustrate this point in Fig. 1(a) for the noninteracting resonant-level model (RLM), describing a single fermionic level coupled by hybridization to a conduction band (see Sec. V for an explicit definition of the model). Abruptly shifting the energy of the level and tracking the time evolution of the level occupancy $n_d(t)$, we compare the TD-NRG to an exact analytical solution for a continuous bath [given by Eq. (50) of Ref. 31] as well as to an exact numerical solution on the Wilson chain using exact diagonalization of the single-particle eigenmodes. Only minuscule deviations are found between the TD-NRG and the exact solution on the Wilson chain, both of which significantly depart at some point from the continuum-limit result. As analyzed in Ref. 31, one can decrease the deviations from the continuum limit and delay them to a later time by reducing the Wilson discretization parameter Λ. At the same time, the deviations are hardly affected by prolonging the chain length N.

This leads to two important conclusions: (i) the main source of error in the TD-NRG is extrinsic rather than intrinsic[31] and (ii) the exponentially decaying tight-binding matrix elements, which lie at the heart of the NRG,[16] are also the limiting factor for reproducing the continuum-limit result for the quench dynamics.

To understand the source of the deviations from the continuum-limit result, we note that globally conserved quantities such as the charge or the spin of the system are locally connected by the continuity equation to associated charge and spin currents. The exponentially decreasing tight-binding matrix elements along the Wilson chain significantly slow down the propagation of such currents,[37] generating internal reflections at the sites of the one-dimensional chain. This is depicted in Fig. 1(b), where we plot the exact time-dependent occupancies of the first 26 sites along the chain in response to a sudden quench of the impurity level. The two-dimensional contour plot clearly reveals reflections of the charge current at certain positions and certain characteristic times. Once the reflected currents reach the impurity site its level occupancy starts to deviate significantly from the exact continuum-limit result. Indeed, the red arrows in Fig. 1(b) indicate instances in time when reflected charge wave fronts reach

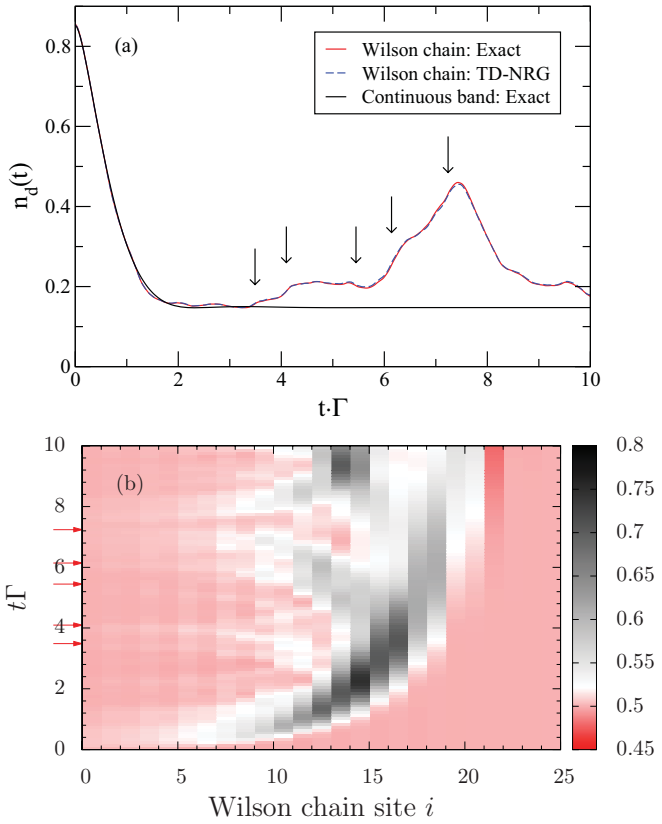

FIG. 1. (Color online) (a) Real-time dynamics of the impurity charge $n_d(t)$ in the resonant-level model following a sudden quench of the level energy from $E_d = -2\Gamma_0$ to $E_d = 2\Gamma_0$ at time $t = 0$. The red solid line shows the exact time evolution on the Wilson chain, obtained by exact diagonalization of the single-particle eigenmodes. The dashed blue line depicts the TD-NRG result, while the solid black line shows the exact analytical solution for a continuous band [given by Eq. (50) of Ref. 31]. (b) A two-dimensional contour plot of the exact time-dependent occupancies $n_i(t)$ of the first 26 sites along the Wilson chain, labeled $i = 0, \ldots, 25$. The red arrows indicate instances in time when reflected currents reach the impurity site. The very same times are marked by the black arrows in panel (a). Parameters: $\Lambda = 1.8$, $\Gamma_0/D = 10^{-2}$, the number of states kept in the TD-NRG is $N_s = 800$, and the chain length is $N = 40$.

the impurity site. At these very same times, the occupancy on the impurity level develops new structures [marked by the black arrows in Fig. 1(a)] that are absent in the continuum limit. Upon decreasing the Wilson discretization parameter Λ the magnitude of the reflected currents is suppressed and the reflection points are pushed deeper down the chain, however, the effect is never fully eliminated as long as $\Lambda > 1$.

An alternative perspective on the effect of the Wilson discretization procedure is provided by examining the exact single-particle energy levels of the RLM. For an ordinary tight-binding chain of length N with a constant hopping matrix element ξ, the single-particle energy levels are roughly uniformly distributed in the energy range $[-D, D]$, where $D = 2\xi$ is the conduction-electron bandwidth. As the chain length is increased, the energy levels become more densely distributed until a continuous spectrum is recovered for $N \to \infty$. A different picture applies to the Wilson chain. As depicted

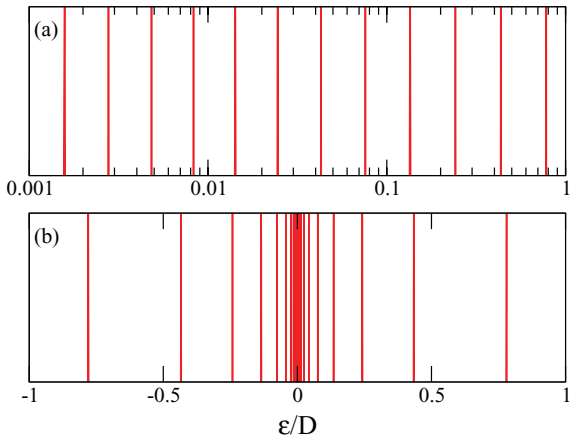

FIG. 2. (Color online) The exact single-particle energy levels of the RLM on a Wilson chain with $\Lambda = 1.8$, $\Gamma_0/D = 10^{-2}$, and $E_d = 0$. The chain length is $N = 40$. Panel (a) depicts positive energies on a logarithmic scale. Panel (b) shows the full spectrum on a linear scale.

in Fig. 2, the single-particle energy levels are uniformly distributed on a logarithmic scale, resulting in a sparse distribution of levels at higher energies. Enumerating the positive single-particle energy levels from high to low, these scale as $\epsilon_n \propto \Lambda^{-n}$, in accordance with Wilson's logarithmic discretization of the conduction band.[16] By prolonging the chain length N one increases the total number of levels, yet the distribution of high-energy levels retains its sparse form even as $N \to \infty$. A continuous band is recovered only upon implementing the combined limit $\Lambda \to 1^+$, $N \to \infty$, which illustrates the limitation of working with a fixed $\Lambda > 1$.[38]

These argumentations clearly point to an intrinsic tradeoff within the TD-NRG, as the very same logarithmic discretization that enables access to exponentially long time scales also prevents from fully recovering the continuum limit. The question then arises whether one can somehow reconcile these two apparently contradicting properties, which is one of the main goals of this work.

B. Plan of the paper

Briefly stated, the aim of this paper is a two-fold extension of the TD-NRG. The first goal is to devise a flexible framework for hybridizing the TD-NRG with complementary methods of calculating real-time dynamics that do not rely on the special structure of the Wilson chain. By liberating ourselves from working on the Wilson chain at all time scales, the hybrid method should enable a systematic improvement of both finite-size and discretization errors.

The second objective is to extend the method from a single quantum quench to repeated switchings between two distinct Hamiltonians $\mathcal{H}^a$ and $\mathcal{H}^b$. Besides being of considerable interest on its own right, this protocol can be viewed as a first vital step toward treating a general time-dependent Hamiltonian $\mathcal{H}(t)$. Indeed, discretizing the time axis and replacing $\mathcal{H}(t)$ within each time interval i with the constant form $\mathcal{H}_i$, the full time evolution can be interpreted as a sequence of quenches.

Despite its conceptual simplicity, this strategy has not been pursued thus far since the initial nonequilibrium density operator $\hat{\rho}_i$ at the beginning of each time interval is neither explicitly known nor of the analytical form required by the original TD-NRG formulation.[31]

To this end, we derive the hybrid-NRG in Sec. II. Since the formulation relies heavily on the TD-NRG, we shall commence in Sec. II A with a brief review of the TD-NRG following Ref. 31. This exposition is essential not only for keeping the paper self-contained, but mainly for introducing the notations and tools that will be used throughout our construction of the hybrid-NRG. After setting the stage in Sec. II A, we present the first major conceptual result of this paper in Sec. II B: the hybrid-NRG approach. The key idea is to partition the Wilson chain into two parts: the high-energy part is treated with the TD-NRG while the low-energy part is fed into the complementary method of choice. The standard TD-NRG approach can be embedded into this more general hybrid framework by shifting the partition to the end of the Wilson chain. In order to make contact with the complementary approach used for hybridizing with the TD-NRG (e.g., the CET), we examine the interface with the TD-NRG from a wave-function perspective in Sec. II B 2.

Using the central results of Sec. II, we extend the hybrid approach to periodic switching between two Hamiltonians in Sec. III, making the simulation of coherent control by an external field accessible to the hybrid method. This section covers the second major conceptual result of this paper. Since the exact evaluation of the reduced density matrix of an arbitrary density operator has remained a computational challenge, we propose a set of approximations that neglect some of the high-energy contributions to the real-time dynamics. These approximations are systematic and are carefully analyzed. The complementary method used to supplement the TD-NRG in this paper, the Chebyshev expansion technique,[28,29] is reviewed in Sec. IV.

Since the deviations of finite-size nonequilibrium dynamics from the continuum limit are linked to the bath discretization, our hybrid framework targets the liberation of numerical simulations from the particular form of the Wilson chain without losing access to exponentially long time scales. In Sec. V, we demonstrate the potential of our hybrid framework by investigating the influence of different hybrid chain types on the discretization errors encountered in the local dynamics. In Sec. VI, we present our results for periodic switching. Since the TD-NRG is embedded in our hybrid framework, we first discuss in Sec. VI A 1 the limitations of a simple extension of the TD-NRG to periodic switching. The exact solution of the finite-size RLM subject to a periodic drive is used to benchmark both the hybrid NRG-CET and the periodic TD-NRG.

The interacting resonant-level model[39–43] (IRLM) serves as a first nontrivial test of our hybrid approach. It includes an additional local capacitive coupling U between the charge on the impurity level and the fermionic band, preventing an exact solution of its dynamics. The low-energy fixed point of the IRLM is identical to that of the noninteracting RLM, featuring a renormalized, U-dependent hybridization strength. By comparing the real-time dynamics of both models with identical renormalized hybridization strengths, we show in Sec. VI B that the local charge dynamics significantly deviates with increasing U from the noninteracting case. Interaction-induced oscillations are found in the IRLM, whose characteristic frequency depends only on the renormalized hybridization and not directly on U. Those oscillations are completely absent in the noninteracting RLM, even though both models share the same low-energy fixed point. Using a strong-coupling analysis, we provide a simple physical picture for this surprising effect. Finally, we conclude with a discussion and outlook in Sec. VII.

II. THE HYBRID-NRG

A. The time-dependent NRG

The TD-NRG has been designed to track the real-time dynamics of quantum-impurity systems following an abrupt quantum quench. The perturbations under consideration are implicitly assumed to be of local character, i.e., perturbations that are applied either to the impurity itself or to its close vicinity.

The Hamiltonian of a quantum-impurity system has the generic structure

$$\mathcal{H} = \mathcal{H}_{\text{bath}} + \mathcal{H}_{\text{imp}} + \mathcal{H}_{\text{mix}}, \tag{1}$$

where $\mathcal{H}_{\text{bath}}$ models the continuous bath, $\mathcal{H}_{\text{imp}}$ represents the decoupled impurity, and $\mathcal{H}_{\text{mix}}$ describes the coupling between the two subsystems. The entire system is characterized at time $t = 0$ by the density operator

$$\hat{\rho}_0 = \frac{e^{-\beta\mathcal{H}^i}}{\text{Tr}(e^{-\beta\mathcal{H}^i})}, \tag{2}$$

when a static perturbation $\Delta\mathcal{H}$ is suddenly switched on: $\mathcal{H}(t \geqslant 0) = \mathcal{H}^i + \Delta\mathcal{H} \equiv \mathcal{H}^f$. The density operator evolves thereafter in time according to

$$\hat{\rho}(t > 0) = e^{-it\mathcal{H}^f}\hat{\rho}_0 e^{it\mathcal{H}^f}. \tag{3}$$

Our objective is to use the NRG to compute the time-dependent expectation value $O(t)$ of a general local operator $\hat{O}$. As shown in Refs. 30 and 31, the result can be written in the form

$$\langle\hat{O}\rangle(t) = \sum_{m}^{N}\sum_{r,s}^{\text{trun}} e^{it(E_r^m - E_s^m)} O_{r,s}^m \rho_{s,r}^{\text{red}}(m), \tag{4}$$

where E_r^m and E_s^m are the dimension-full NRG eigenenergies of the perturbed Hamiltonian at iteration $m \leqslant N$, $O_{r,s}^m$ is the matrix representation of $\hat{O}$ at that iteration, and $\rho_{s,r}^{\text{red}}(m)$ is the reduced density matrix defined in Eq. (10) below. The restricted sum over r and s requires that at least one of these states is discarded at iteration m. The NRG chain length N implicitly defines the temperature entering Eq. (2): $T_N \propto \Lambda^{-N/2}$, where $\Lambda > 1$ is the Wilson discretization parameter.

The derivation of Eq. (4) relies on two key ingredients: (i) the identification of a complete basis set of approximate NRG eigenstates for the many-body Fock space $\mathcal{F}_N$ of the Wilson chain and (ii) expectation values are obtained by explicitly tracing over this complete basis set using a suitable resummation procedure. Below, we review these two

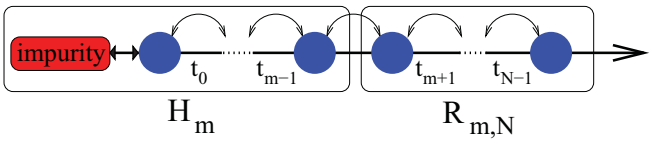

FIG. 3. (Color online) The full Wilson chain of length N is divided into a subchain of length m and the "environment" $R_{m,N}$. The Hamiltonian $\mathcal{H}_m$ can be viewed either as acting only on the subchain of length m or as acting on the full chain of length N, but with the hopping matrix elements $t_m,\ldots,t_{N-1}$ all set to zero. The former picture is the traditional one. In the TD-NRG, one adopts the latter point of view.

key components following the notations and presentation of Ref. 31.

1. Complete basis set

The NRG targets an iterative solution of a quantum impurity coupled to a finite Wilson chain with N chain links.[44] Similar to the initial sweep in the finite-size DMRG, one can view the NRG procedure as a set of operations, where at first all hopping matrix elements are set to zero along the N-site chain, and at each successive step, another hopping matrix element is switched on. The full Hamiltonian $\mathcal{H}_N$ is recovered once all hopping matrix elements have been switched on. The entire sequence of Hamiltonians $\mathcal{H}_m$ with $m \leqslant N$ act in this picture on the same Fock space $\mathcal{F}_N$ of the N-site chain, hence each NRG eigenenergy of $\mathcal{H}_m$ has an extra degeneracy of $d^{(N-m)}$, where d is the number of distinct configurations at each site along the chain. The extra degeneracy stems from the $N-m$ "environment" sites at the end of the chain, denoted by $R_{m,N}$ in Fig. 3, which remain decoupled from the impurity at iteration m.

When acting on the m-site chain, we label the NRG eigenstates and eigenenergies of $\mathcal{H}_m$ by $\{|r;m\rangle\}$ and E_r^m, respectively. Consider now the action of $\mathcal{H}_m$ on the full N-site chain. Enumerating the different configurations of site i by $\{\alpha_i\}_{i=1,\ldots,d}$, each of the tensor-product states $|r;m\rangle\otimes|\alpha_{m+1},\ldots,\alpha_N\rangle$ with arbitrary $\alpha_{m+1},\ldots,\alpha_N$ is a degenerate NRG eigenstate of $\mathcal{H}_m$ with energy E_r^m. To label these states, we introduce the shorthand notation $|r,e;m\rangle$, where the "environment" variable $e=\{\alpha_{m+1},\ldots,\alpha_N\}$ encodes the $N-m$ site labels $\alpha_{m+1},\ldots,\alpha_N$, and the index m is used to record where the chain is partitioned into a "subsystem" and an "environment" (see Fig. 3).

In order to retain a manageable number of states, the high-energy eigenstates are discarded after each iteration, which is fully justified in equilibrium by the hierarchy of the energy scales along the Wilson chain and the Boltzmann form of the equilibrium density operator. Regarding all states of the final iteration as discarded, it has been show in Refs. 30 and 31 that the collection of all states discarded in the course of the NRG iterations form a complete basis set of approximate NRG eigenstates for the full N-site chain.

To understand this important point, consider the first iteration $m_{\min}$ at which states are discarded. In order to keep track of the complete basis set of the N-site chain, the eigenstates $|r,e;m_{\min}\rangle$ can be formally divided into two distinct subsets: the discarded high-energy states labelled $\{|l,e;m_{\min}\rangle_{\rm dis}\}$ and the kept low-energy states labelled $\{|k,e;m_{\min}\rangle_{\rm kp}\}$. Obviously, the sum of the two subsets forms a complete basis set of the full chain. To simplify the notations, we shall omit hereafter the subscripts "dis" and "kp," and will use in exchange the indices l and k to label the discarded and kept states, respectively. At the next NRG iteration only the kept states are used to construct the NRG eigenstates of $\mathcal{H}_{m_{\min}+1}$ within the truncated subspace spanned by $\{|k,e;m_{\min}\rangle\}$. The resulting NRG eigenstates can again be divided into two subsets of discarded and kept states which, when combined with the discarded eigenstates of iteration $m_{\min}$, form a complete basis set of the Fock space $\mathcal{F}_N$ of the full N-site chain. Repeating this procedure at all subsequent iterations, one continues to maintain a complete basis set of $\mathcal{F}_N$ up to the final NRG iteration $m=N$. In this manner, we arrive at the following completeness relation:

$$\sum_{m=m_{\min}}^{N}\sum_{l,e}|l,e;m\rangle\langle l,e;m| = \sum_{m=m_{\min}}^{N}\hat{P}_m = 1, \tag{5}$$

where the summation over m starts from the first iteration $m_{\min}$ at which a basis-set reduction is imposed. Here, the summation indices l and e implicitly depend on m, and the projector onto the subspace discarded at iteration $m_{\min}\leqslant m\leqslant N$ is defined as

$$\hat{P}_m = \sum_{l,e}|l,e;m\rangle\langle l,e;m|. \tag{6}$$

The complementary projector $\hat{1}_m^+$ onto the subspace retained at iteration m ($m<N$) is given in turn by

$$\hat{1}_m^+ = \sum_{k,e}|k,e;m\rangle\langle k,e;m|, \tag{7}$$

which can be recast in the form

$$\hat{1}_m^+ = \sum_{m'=m+1}^{N}\hat{P}_{m'}. \tag{8}$$

This latter equality reflects the fact that all states retained at iteration m are necessarily discarded at some later iteration m'. In particular, since all states of the final iteration N are regarded discarded, then $\hat{1}_N^+$ is identically zero while $\hat{1}_{N-1}^+$ coincides with $\hat{P}_N$. Combined with Eq. (8), the completeness relation of Eq. (5) can further be partitioned into

$$1 = \sum_{m=m_{\min}}^{M}\hat{P}_m + \hat{1}_M^+ \tag{9}$$

with arbitrary $m_{\min}\leqslant M\leqslant N$. This useful identity will be repeatedly used in constructing the hybrid-NRG.

2. Reduced density matrix and the TD-NRG algorithm

Following a sudden quench, the time evolution of the system is governed by the perturbed Hamiltonian $\mathcal{H}^f$ while the initial condition is encoded in the initial density matrix $\hat{\rho}_0$. For quantum-impurity systems, all relevant information on

the initial condition is contained in Eq. (4) in the form of the reduced density matrices[30,31] $\rho^{\rm red}_{s,r}(m)$, defined as

$$\rho^{\rm red}_{s,r}(m) = \sum_e \langle s,e;m|\hat{\rho}_0|r,e;m\rangle. \tag{10}$$

Here, the states $|r,e;m\rangle$ and $|s,e;m\rangle$ correspond to the Hamiltonian $\mathcal{H}^f$, and the summation runs over the environment degrees of freedom e. The only approximation entering Eq. (4) is the standard NRG approximation $\mathcal{H}_N|r,e;m\rangle \approx \mathcal{H}_m|r,e;m\rangle = E^m_r|r,e;m\rangle$, which enables us to write

$$\langle s,e;m|\hat{\rho}(t)|r,e;m\rangle = e^{it(E^m_r - E^m_s)}\langle s,e;m|\hat{\rho}_0|r,e;m\rangle. \tag{11}$$

Apart from this sole point, Eq. (4) constitutes an exact evaluation of $O(t)$ on the discretized N-site chain.

Practical calculations hinge on the ability to accurately compute the reduced density matrices of Eq. (10). For a general $\hat{\rho}_0$ this can be a daunting task. However, in the case of interest where $\hat{\rho}_0$ has the standard Boltzmann form of Eq. (2), the summation over e can be carried out exactly. Hence $\rho^{\rm red}_{s,r}(m)$ can be evaluated at the same level of accuracy as the equilibrium density operator $\hat{\rho}_0$. Technically, this goal is achieved by implementing two independent NRG runs, one for the initial Hamiltonian $\mathcal{H}^i$ in order to construct $\hat{\rho}_0$ using Eq. (2), and another for the full Hamiltonian $\mathcal{H}^f$. The reduced density matrix $\rho^{\rm red}_{s,r}(m)$ is first evaluated with respect to the eigenstates of the initial Hamiltonian, and then rotated[30,31] to the eigenstates of the full Hamiltonian using the overlap matrices

$$\langle q_i;m|r;m\rangle = S_{q_i,r}(m). \tag{12}$$

Here, $|r;m\rangle$ denotes an NRG eigenstate of the full Hamiltonian at iteration m, and $|q_i;m\rangle$ is an NRG eigenstate of the initial Hamiltonian at the same iteration. The method of calculating the overlap matrices $S_{q_i,r}(m)$ is detailed in Ref. 31.

B. Derivation of the hybrid-NRG

The original TD-NRG approach, summarized above, tracks the quench dynamics of a quantum-impurity system in terms of the phase factors $e^{it(E^m_r - E^m_s)}$ and the reduced density matrices $\rho^{\rm red}_{s,r}(m)$ assigned to each NRG iteration m. Although quite elegant and useful, it is less transparent how to incorporate ideas from methods such as the TD-DMRG or CET, as these deal with wave functions directly. To develop a convenient and flexible interface between the TD-NRG and these vastly different approaches, we reformulate the former approach from a wave-function perspective.

1. Wave-function formulation

Let us commence with accurately stating the problem from a wave-function perspective. We are interested in tracking the time evolution of some initial state $|\psi_0\rangle$ under the dynamics defined by the Hamiltonian $\mathcal{H}$ acting on a finite Wilson chain of length N. We shall not concern ourselves at this stage with how the initial state $|\psi_0\rangle$ is generated, but will elaborate on this important point later on.

Formally, our task boils down to computing

$$|\psi(t)\rangle = e^{-i\mathcal{H}t}|\psi_0\rangle\ . \tag{13}$$

Application of the completeness relation of Eq. (9) to the state $|\psi(t)\rangle$ leads to its partitioning according to

$$|\psi(t)\rangle = \sum_{m=m_{\rm min}}^{M} |\phi_m(t)\rangle + |\chi_M(t)\rangle\ , \tag{14}$$

where

$$|\phi_m(t)\rangle = \hat{P}_m|\psi(t)\rangle \tag{15}$$

and

$$|\chi_M(t)\rangle = \hat{1}^+_M|\psi(t)\rangle \tag{16}$$

are the projections of $|\psi(t)\rangle$ onto the subspaces defined by $\hat{P}_m$ and $\hat{1}^+_M$, respectively. Equation (14) simply converts the general state $|\psi(t)\rangle$ into a concrete representation in terms of our complete basis set.

2. Evaluation of expectation values

Given the time-evolved wave function of Eq. (14), we proceed to compute time-dependent averages of physical observables:

$$A(t) = \langle\psi(t)|\hat{A}|\psi(t)\rangle. \tag{17}$$

To this end, we use the completeness relation of Eq. (9) to decompose any arbitrary operator $\hat{A}$ into

$$\hat{A} = \sum_{m,m'}^{M} \hat{P}_m\hat{A}\hat{P}_{m'} + \sum_{m}^{M}(\hat{P}_m\hat{A}\hat{1}^+_M + \hat{1}^+_M\hat{A}\hat{P}_m) + \hat{1}^+_M\hat{A}\hat{1}^+_M, \tag{18}$$

where the summations over m and m' start from $m_{\rm min}$. Writing the first two terms on the right-hand side of Eq. (18) as

$$\sum_{m=m_{\rm min}}\left[\hat{P}_m\hat{A}\hat{P}_m + \hat{P}_m\hat{A}\left(\sum_{m'=m+1}^{M}\hat{P}_{m'} + \hat{1}^+_M\right) + \left(\sum_{m'=m+1}^{M}\hat{P}_{m'} + \hat{1}^+_M\right)\hat{A}\hat{P}_m\right] \tag{19}$$

and noting that

$$\hat{1}^+_m = \sum_{m'=m+1}^{M}\hat{P}_{m'} + \hat{1}^+_M, \tag{20}$$

the operator $\hat{A}$ is recast in the exact form

$$\hat{A} = \sum_{m=m_{\rm min}}^{M}\hat{A}(m) + \hat{A}_\chi, \tag{21}$$

where

$$\hat{A}(m) = \hat{P}_m\hat{A}\hat{P}_m + \hat{1}^+_m\hat{A}\hat{P}_m + \hat{P}_m\hat{A}\hat{1}^+_m \tag{22}$$

and

$$\hat{A}_\chi = \hat{1}^+_M\hat{A}\hat{1}^+_M\ . \tag{23}$$

Here, the index M can take any value in the range $m_{\rm min} \leqslant M \leqslant N$. Explicitly, the operator $\hat{A}(m)$ has the formal representation

$$\hat{A}(m) = \sum_{r,s}^{\rm trun}\sum_{e,e'}|r,e;m\rangle\langle r,e;m|\hat{A}|s,e';m\rangle\langle s,e';m|, \tag{24}$$

where the restricted sum $\sum_{r,s}^{\text{trun}}$ implies, as before, that at least one of the states r and s is discarded at iteration m.

As in the original TD-NRG, we focus hereafter on local operators $\hat{A}$ that act solely on degrees of freedom that reside either on the impurity itself or on the first $m_{\min}$ sites along the Wilson chain.[31] For any such local operator, the matrix elements in Eq. (24) are diagonal in and independent of the environment variables e and e':

$$\langle r,e;m|\hat{A}|s,e';m\rangle = A^m_{r,s}\delta_{e,e'}. \tag{25}$$

Substituting the operator decomposition of Eq. (21) into Eq. (17) and using the definition $|\chi_M(t)\rangle = \hat{1}^+_m|\psi(t)\rangle$ of Eq. (16), the time-dependent expectation value takes the form

$$A(t) = \sum_{m=m_{\min}}^{M} \langle\psi(t)|\hat{A}(m)|\psi(t)\rangle + \langle\chi_M(t)|\hat{A}|\chi_M(t)\rangle. \tag{26}$$

This general expression reduces for a local operator to

$$A(t) = \langle\chi_M(t)|\hat{A}|\chi_M(t)\rangle + \sum_{m=m_{\min}}^{M}\sum_{r,s}^{\text{trun}} A^m_{r,s}\rho^m_{s,r}(t), \tag{27}$$

where

$$\rho^m_{s,r}(t) = \sum_e \langle s,e;m|\psi(t)\rangle\langle\psi(t)|r,e;m\rangle \tag{28}$$

is the reduced density matrix at iteration m.

Three comments should be made about Eqs. (27) and (28). First, these expressions are both general and exact for the real-time dynamics on the discretized chain. Apart from the restriction to local operators, no further approximations or assumptions are involved. Second, Eqs. (27) and (28) can be easily extended to a statistical admixture of initial states $\{|\psi_i\rangle\}$ with the statistical weights $\{w_i\}$. This requires the simple substitutions

$$\langle\chi_M(t)|\hat{A}|\chi_M(t)\rangle \to \sum_i w_i\langle\chi_{M,i}(t)|\hat{A}|\chi_{M,i}(t)\rangle \tag{29}$$

and

$$\hat{\rho}(t) = |\psi(t)\rangle\langle\psi(t)| \to \sum_i w_i|\psi_i(t)\rangle\langle\psi_i(t)| \tag{30}$$

in Eqs. (27) and (28), respectively. Third, the conventional TD-NRG approach is recovered from Eqs. (27) and (28) by (i) setting $M = N$, (ii) realizing that $\hat{A}_\chi = 0$ for $N = M$, and (iii) adopting the standard NRG approximation $\mathcal{H}|r,e;m\rangle \approx E^m_r|r,e;m\rangle$, which simplifies $\rho^m_{s,r}(t)$ to $e^{i(E^m_r - E^m_s)t}\rho^{\text{red}}_{s,r}(m)$ with

$$\rho^{\text{red}}_{s,r}(m) = \sum_e \langle s,e;m|\psi_0\rangle\langle\psi_0|r,e;m\rangle. \tag{31}$$

A natural generalization of the TD-NRG is to apply the NRG approximation $\mathcal{H}|r,e;m\rangle \approx E^m_r|r,e;m\rangle$ to the early iterations $m \leqslant M$ only, converting Eqs. (27) and (28) to

$$A(t) = \sum_{m=m_{\min}}^{M}\sum_{r,s}^{\text{trun}} e^{i(E^m_r - E^m_s)t}A^m_{r,s}\rho^{\text{red}}_{s,r}(m) + \langle\chi_M(t)|\hat{A}|\chi_M(t)\rangle. \tag{32}$$

This equation, which constitutes one of the central results of this paper, interpolates between the TD-NRG, corresponding to $M = N$, and the exact time-dependent expectation value, obtained for $M = m_{\min}$. Of course, the latter statement assumes an exact evaluation of $|\chi_M(t)\rangle$, which is an impractical task for $M = m_{\min}$. As discussed below, a proper choice of the parameter M allows for an improved evaluation of $|\chi_M(t)\rangle$ using alternative methods such as the TD-DMRG or CET, with minimal loss of accuracy at the early iterations to which the NRG approximation is applied. Furthermore, by resorting to methods that do not rely on the special structure of the Wilson chain to evaluate $|\chi_M(t)\rangle$, one can abandon the exponential decay of the hopping matrix elements beyond site M, reducing thereby the discretization errors inherent to the Wilson chain. These principles form the core of the hybrid approach. We now turn to elaborate on the technicalities of how M is selected, the interface with the hybridized method, and the way in which the initial state $|\psi_0\rangle$ is constructed.

C. Interface between the TD-NRG and the hybridized approach

1. *Hierarchy of energy scales and the time evolution of* $|\chi_M(t)\rangle$

To turn Eq. (32) into an operative platform for hybridizing the TD-NRG with alternative methods of computing the real-time dynamics of $|\chi_M(t)\rangle$, it is useful to go back to the partitioning of $|\psi(t)\rangle$ specified in Eq. (14) and gain a deeper insight into the energy scales encoded into the projectors $\hat{P}_m$. Applying the operator decomposition of Eq. (21) to the Hamiltonian $\mathcal{H}$, the latter is written as

$$\mathcal{H} = \sum_{m=m_{\min}}^{M} \mathcal{H}(m) + \hat{h}_\chi, \tag{33}$$

where

$$\mathcal{H}(m) \equiv \hat{P}_m\mathcal{H}\hat{P}_m + \hat{P}_m\mathcal{H}\hat{1}^+_m + \hat{1}^+_m\mathcal{H}\hat{P}_m \tag{34}$$

and

$$\hat{h}_\chi = \hat{1}^+_M\mathcal{H}\hat{1}^+_M. \tag{35}$$

It is rather easy to see that the different Hamiltonian terms that appear in Eq. (33) generally do not commute with one another, i.e., $[\mathcal{H}(m),\hat{h}_\chi] \neq 0$ and $[\mathcal{H}(m),\mathcal{H}(m')] \neq 0$ if $m \neq m'$. According to the NRG philosophy, however, the off-diagonal terms $\hat{P}_m\mathcal{H}\hat{P}_{m'}$ with $m \neq m'$ are expected to be small, as these couple excitations on different energy scales. Consequently, one can approximate $\mathcal{H}(m)$ with $\hat{h}_m = \hat{P}_m\mathcal{H}\hat{P}_m$ to obtain the approximate Hamiltonian

$$\mathcal{H} \approx \sum_{m=m_{\min}}^{M} \hat{h}_m + \hat{h}_\chi. \tag{36}$$

Evidently, Eq. (36) becomes exceedingly more accurate the smaller is M, acquiring the status of an identity for $M = m_{\min}$, since $\mathcal{H} = \hat{h}_\chi$ in this case. Furthermore, since the Hamiltonian terms $\hat{h}_\chi$ and $\hat{h}_m$ with $m \leqslant M$ are confined to the subspaces projected out by $\hat{1}^+_M$ and $\hat{P}_m$, respectively, the Hamiltonian of Eq. (36) is block-diagonal in these subspaces with $[\hat{h}_m,\hat{h}_{m'}] = [\hat{h}_m,\hat{h}_\chi] = 0$. This allows us to write the time-dependent state $|\psi(t)\rangle$ within this approximation as

$$|\psi(t)\rangle = \sum_{m=m_{\min}}^{M} e^{-i\hat{h}_m t}|\phi_m\rangle + e^{-i\hat{h}_\chi t}|\chi_M\rangle, \tag{37}$$

where $|\phi_m\rangle = \hat{P}_m|\psi_0\rangle$ and $|\chi_M\rangle = \hat{1}_M^+|\psi_0\rangle$ are the projections of the initial state onto the subspaces defined by $\hat{P}_m$ and $\hat{1}_M^+$, respectively. In other terms, it suffices in this approximation to first project out $|\chi_M\rangle$ and $|\phi_m\rangle$ from the initial state, and then propagate them separately in time, each according to its own Hamiltonian.

Physically, Eq. (37) prescribes a decomposition of the desired time-dependent state into independent components, each associated with a different time scale $t_m = 1/D_m \sim \Lambda^{m/2}$ and evolving according to its own reduced Hamiltonian (either $\hat{h}_m$ or $\hat{h}_\chi$). In the case of spinless electrons, the reduced Hamiltonian $\hat{h}_m$ has the explicit form

$$\hat{h}_m = \sum_{l,e} E_l^m |l,e;m\rangle\langle l,e;m| + \sum_{n=m}^{N-1} t_n (\hat{P}_m f_{n+1}^\dagger f_n \hat{P}_m + \text{H.c.}), \tag{38}$$

where $f_n^\dagger$ creates an electron on the nth site of the Wilson chain, t_n is the dimension-full hopping matrix element between sites n and $n+1$ along the chain, l runs over the NRG eigenstates discarded at iteration m, and E_l^m denotes their corresponding NRG eigenenergies. Note that the projection operators $\hat{P}_m$ in the right-most term are attached in practice only to f_m and $f_m^\dagger$, as all other operators f_n with $n > m$ do not possess any matrix element that takes us out of the subspace defined by $\hat{P}_m$. The Hamiltonian $\hat{h}_\chi$ is nearly identical, except that the index m is replaced with M and the discarded states $|l,e;m\rangle$ are replaced with the NRG eigenstates retained at the conclusion of iteration M. In the presence of additional bands, the Wilson orbitals $f_n^\dagger$ acquire an additional flavor index ν, which may label the spin σ, an orbital channel α, or the spin-channel tuple $\nu = (\sigma,\alpha)$ as in two-channel Kondo models (see, e.g., Ref. 45). Other than setting $f_n^\dagger \to f_{n\nu}^\dagger$ and adding a suitable summation over ν, the very same equations carry over to the general multiband case.

2. Physical role of the parameter M

The Hamiltonian of Eq. (38) can be interpreted as modeling a hyperimpurity with the localized configurations $|l\rangle$ and eigenenergies E_l^m, which are tunnel coupled to a chain of length $N-m$. The size of the impurity is equal to the number of states discarded at iteration m. Thus the calculation of $|\phi_m(t)\rangle = e^{-ih_m t}|\phi_m\rangle$ becomes exceedingly more affordable the larger is m due to the exponential reduction of the Fock space of the chain $R_{m,N}$ attached to the hyperimpurity. We stress, however, that the dimension of the subspace associated with $\hat{P}_{m_{\min}}$ is comparable in size to that of the full Wilson chain, hence an accurate evaluation of $|\phi_{m_{\min}}(t)\rangle$ is similar in complexity to the calculation of the full state $|\psi(t)\rangle$.

There is little computational gain in implementing Eq. (37) if all components of the wave function must be accurately computed. Fortunately, this generally is not the case for the class of problems of interest, where $|\psi_0\rangle$ is some low-lying eigenstate (typically the ground state) of an initial Hamiltonian $\mathcal{H}^i$. Under these circumstances, $|\psi_0\rangle$ typically has only negligible overlap with the high-energy states of $\mathcal{H}$, i.e., $\langle\phi_m|\phi_m\rangle \ll 1$ for the initial NRG iterations. Overlap becomes significant only upon approaching a characteristic energy scale

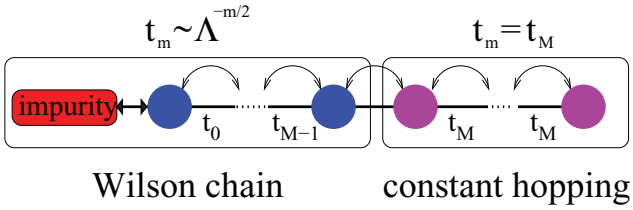

FIG. 4. (Color online) A hybrid Wilson chain where the first $M+1$ hopping matrix elements decrease according to $t_n \propto \Lambda^{-n/2}$ with $\Lambda > 1$, and all further hopping matrix elements are held constant and equal to t_M.

D_M where the spectra of the full and the unperturbed Hamiltonians begin to notably deviate from one another. Usually this happens at some characteristic low-energy scale of the problem, e.g., the Kondo temperature T_K in case of the Kondo Hamiltonian.

Consequently, the initial NRG iterations with $m \leqslant M$ can be treated using further approximations such as setting $t_n = 0$ in Eq. (38), corresponding to the standard NRG approximation. Since the reduced density matrix $\rho_{s,r}^m(t)$ requires only the matrix element $\langle\psi(t)|r,e;m\rangle$, one can implement $e^{i\mathcal{H}t}|r,e;m\rangle$ instead of propagating $|\phi_m(t)\rangle$ in time, which simplifies the exact result of Eq. (27) to the approximate expression of Eq. (32). The computational effort can therefore be focused on evaluating $|\chi_M(t)\rangle$, which dominates the expectation value $A(t)$. Most importantly, given the initial state $|\chi_M\rangle$ and the effective Hamiltonian $\hat{h}_\chi$ generated by the NRG, $|\chi_M(t)\rangle$ can be computed using one's method of choice.

The physical role of the integer M, which so far served as a mere parameter, is now disclosed: it defines the NRG iteration M beyond which the time-dependent state should be accurately computed. Moreover, this partitioning can be used to improve the discrete representation of the continuous bath as noted above. For example, one can design a hybrid chain such that all sites up to $m = M$ are discretized with $\Lambda > 1$ and all further sites are converted to $\Lambda \to 1^+$ (see Fig. 4). Such a chain is impractical for pure NRG-based calculations, but is made possible by resorting to alternative methods for tracking the time evolution of $|\chi_M(t)\rangle$. In this manner, discretization errors are significantly reduced at the energy scale D_M, corresponding to the time scale $t_M = 1/D_M$. The crucial point to notice is that the reduced Hamiltonian h_χ has the effective bandwidth $D_M \propto \Lambda^{-M/2} \ll D$ and acts on a reduced chain of length $N-M$. This enables access to long time scales of order $t_M \gg 1/D$ using techniques such as the TD-DMRG or CET, which otherwise are restricted to far shorter times.

The only remaining uncertainty pertains to a suitable choice of the iteration number M. In the absence of a sharp mathematical criterion, the choice of M should be considered on a case-by-case basis. Qualitatively, one expects the scale D_M to correspond to $\max\{\Gamma_0, |\epsilon_d|\}$ for the resonant-level model [see Eq. (72) below], and to the Kondo temperature[16] T_K for the Kondo model. The case of an Anderson impurity is clearly more subtle, as spin and charge relax on different time scales.[30] Here, a different optimal choice of M may apply to observables acting on the spin and charge sectors.

3. Construction of the initial state $|\psi_0\rangle$

So far, we have assumed the decomposition of the initial state $|\psi_0\rangle$ according to Eq. (14) but did not specify how $|\psi_0\rangle$ is obtained in practice. The construction of $|\psi_0\rangle$ and its projection $|\chi_M\rangle$ onto the low-energy subspace defined by $\hat{1}^+_M$ depends in detail on the method hybridized with the TD-NRG. Our discussion below covers both the TD-DMRG and CET.

We begin with the initial NRG run, which provides us with the low-energy Hamiltonian $\hat{h}^i_\chi = \hat{1}^+_{i,M}\mathcal{H}^i\hat{1}^+_{i,M}$ corresponding to the initial Hamiltonian $\mathcal{H}^i$. Here, $\hat{1}^+_{i,M}$ denotes the projection operator onto the low-energy subspace of $\mathcal{H}^i$ retained at the conclusion of iteration M. As detailed in Eq. (38), $\hat{h}^i_\chi$ comprises a hyperimpurity, a residual chain of length $N-M$, and a tunnel coupling between both parts of the system. In the next step, the ground state $|\psi_0\rangle$ of $\hat{h}^i_\chi$ is computed. In case of the TD-DMRG, this is done using the standard DMRG algorithm,[46] while for the CET (for which a shorter chain $R_{M,N}$ is employed) the Davidson method[47] can be used. At the conclusion of this step one has the initial state $|\psi_0\rangle$ at hand, expressed via the kept NRG eigenstates of $\mathcal{H}^i_M$:

$$|\psi_0\rangle = \sum_{k_i,e} c_{k_i,e}|k_i,e;M\rangle. \tag{39}$$

Given $|\psi_0\rangle$, the state $|\chi_M\rangle$ is obtained by projecting $|\psi_0\rangle$ onto the low-energy subspace of the full Hamiltonian defined by $\hat{1}^+_M$. This in turn yields

$$|\chi_M\rangle = \sum_{k,e} b_{k,e}|k,e;M\rangle \tag{40}$$

with

$$b_{k,e} = \sum_{k_i} S^*_{k_i,k}(M)c_{k_i,e}, \tag{41}$$

where $S(M)$ is the overlap matrix defined in Eq. (12). This state is then propagated in time according to $|\chi_M(t)\rangle = e^{-i\hat{h}_\chi t}|\chi_M\rangle$ using either the TD-DMRG or CET and fed into Eq. (32). As for the reduced density matrices $\rho^{\rm red}_{s,r}(m)$ entering Eq. (32), these are computed recursively from $|\psi_0\rangle$ using the standard TD-NRG algorithm.[31]

III. REPEATED SWITCHINGS

Armed with the hybrid-NRG platform, we proceed in this section to the second major result of this paper—the extension of the TD-NRG from a single quantum quench to repeated switching events.

Coherent control of small nanodevices such as semiconductor quantum dots or superconducting flux qubits can be achieved by applying gate-voltage pulses or time-dependent electromagnetic fields. For example, circularly polarized laser pulses are used to induce and control the spin polarization in semiconductor quantum dots.[48] Alternatively, one can apply rapid changes to close-by gate voltages in order to control the energy levels and/or the tunneling rates of a quantum dot. Each of these protocols involves repeated switchings between two distinct configurations of the applied fields, which we denote hereafter by a and b. Theoretically this corresponds to periodic conversions in time between two quantum-impurity Hamiltonians, $\mathcal{H}^a$ and $\mathcal{H}^b$, that differ in those components describing the isolated dot and its coupling to the leads. Our goal is to track the time evolution of local expectation values in response to such a sequence of switching events.

To clearly formulate the problem, we assume that the system resides at time $t=0$ in a low-lying eigenstate of the Hamiltonian $\mathcal{H}^a$, when its Hamiltonian is abruptly converted from $\mathcal{H}^a$ to $\mathcal{H}^b$. The system then evolves in time under the influence of $\mathcal{H}^b$ up to time $\tau > 0$, when the Hamiltonian of the system is suddenly switched back to $\mathcal{H}^a$ for the duration $\tau < t < 2\tau$. This sequence of switchings is repeated periodically with a period of 2τ, as described by the time-dependent Hamiltonian

$$\mathcal{H}(t>0) = \begin{cases} \mathcal{H}^a, & (2n-1)\tau \leqslant t < 2n\tau, \\ \mathcal{H}^b, & 2n\tau \leqslant t < (2n+1)\tau \end{cases} \tag{42}$$

(here $n = 0,1,2,\ldots$). Within each time interval where the Hamiltonian is constant, the expectation value of a general local operator $\hat{A}$ is given by Eqs. (27) and (28) where, depending on the time interval in question, $|\chi_M(t)\rangle$ and $\rho^m_{s,r}(t)$ pertain either to $\mathcal{H}^a$ or $\mathcal{H}^b$. Explicitly, $|\chi_M(t)\rangle$ is replaced with $|\chi^{(\alpha)}_M(t)\rangle = 1^+_{\alpha,M}|\psi(t)\rangle$, where $1^+_{\alpha,M}$ denotes the projection operator of Eq. (7) written with respect to NRG eigenstates of $\mathcal{H}^\alpha$ ($\alpha = {\rm a,b}$). With these adjustments, the resulting expression is formally exact, but requires explicit knowledge of the states $|\psi(t)\rangle$ and $|\chi^{(\alpha)}_M(t)\rangle$.

Consider a particular time interval $(2n-1)\tau < t < 2n\tau$ in which the system evolves according to the Hamiltonian $\mathcal{H}^a$. As discussed in Sec. II B 2, the expectation value $A(t)$ can be approximated by applying the conventional NRG approximation to the early iterations $m \leqslant M$ only. This yields Eq. (32), where $|\chi_M(t)\rangle$, the eigenenergies E^m_r and E^m_s, and the state labels s and r correspond to $\mathcal{H}^a$. The only formal modification as compared to Eq. (32) pertains to the reduced density matrix $\rho^{\rm red}_{s,r}(m)$, in which the initial state $|\psi_0\rangle$ must be replaced with $|\psi(t)\rangle$ at time $t_{2n-1} = (2n-1)\tau$. The same set of rules carry over to any given time interval $2n\tau < t < (2n+1)\tau$, except that $\mathcal{H}^a$ is replaced with $\mathcal{H}^b$, and the initial state $|\psi_0\rangle$ is replaced with $|\psi(t)\rangle$ at time $t_{2n} = 2n\tau$. This leaves us with those instances in time where the Hamiltonian is abruptly converted from $\mathcal{H}^a$ to $\mathcal{H}^b$ or vice versa.

For concreteness let us focus on the time instance $t_{2n} = 2n\tau$, when the Hamiltonian is converted from $\mathcal{H}^a$ to $\mathcal{H}^b$. As described in Eq. (14), the state of the system can be formally decomposed within the time interval $(2n-1)\tau < t < 2n\tau$ into

$$|\psi(t)\rangle = \left|\chi^{(\rm a)}_M(t)\right\rangle + |\delta\psi^{(\rm a)}(t)\rangle \tag{43}$$

with $|\delta\psi^{(\rm a)}(t)\rangle = \sum_{m\leqslant M}|\phi^{(\rm a)}_m(t)\rangle$. Here, the states $|\phi^{(\rm a)}_m(t)\rangle$ are projected according to the NRG eigenstates of $\mathcal{H}^a$. The time-dependent density operator is next divided into $\hat{\rho}^{(\rm a)}_\chi(t) + \delta\hat{\rho}^{(\rm a)}(t)$, where

$$\hat{\rho}^{(\rm a)}_\chi(t) = \left|\chi^{(\rm a)}_M(t)\right\rangle\left\langle\chi^{(\rm a)}_M(t)\right| \tag{44}$$

and $\delta\hat{\rho}^{(\rm a)}(t) = \hat{\rho}(t) - \hat{\rho}^{(\rm a)}_\chi(t)$. Setting $t \to t_{2n}$ and replacing $\hat{\rho}_0 = |\psi_0\rangle\langle\psi_0| \to |\psi(t_{2n})\rangle\langle\psi(t_{2n})|$ in Eq. (10), the reduced

density matrix with respect to the eigenstates of $\mathcal{H}^a$ reads

$$\rho^{\mathrm{red\,(a)}}_{s,r}(m) = \underbrace{\sum\nolimits_e \langle s,e;m|\hat{\rho}^{(\mathrm{a})}_{\chi}(t_{2n})|r,e;m\rangle}_{\chi^{(\mathrm{a})}_{s,r}(m)} + \delta\rho^{(\mathrm{a})}_{s,r}(m), \tag{45}$$

where we have defined

$$\delta\rho^{(\mathrm{a})}_{s,r}(m) \equiv \sum_e \langle s,e;m|\delta\hat{\rho}^{(\mathrm{a})}(t_{2n})|r,e;m\rangle. \tag{46}$$

An equivalent expression $\rho^{\mathrm{red\,(b)}}_{s,r}(m) = \chi^{(\mathrm{b})}_{s,r}(m) + \delta\rho^{(\mathrm{b})}_{s,r}(m)$ applies to the reduced density matrix with respect to the NRG eigenstates of the Hamiltonian $\mathcal{H}^b$.

In the notations of Ref. 31 [see Eqs. (31) and (32) therein], the first term $\chi^{(\mathrm{a})}(m)$ in Eq. (45) is of the pure form $\chi^{++}(m)$, having none of the components $\chi^{+-}(m)$, $\chi^{-+}(m)$, and $\chi^{--}(m)$. Thus one has the exact conversion[31]

$$\chi^{(\mathrm{b})}(m) = S^\dagger(m)\,\chi^{(\mathrm{a})}(m)\,S(m), \tag{47}$$

where $S(m)$ is the overlap matrix between the NRG eigenstates of $\mathcal{H}^a$ and $\mathcal{H}^b$ defined by Eq. (12). By contrast, the second term $\delta\rho^{(\mathrm{a})}(m)$ in Eq. (45) involves all four components $\delta\rho^{++}(m)$, $\delta\rho^{+-}(m)$, $\delta\rho^{-+}(m)$, and $\delta\rho^{--}(m)$, and as a result lacks an explicit relation[31] to $\delta\rho^{(\mathrm{b})}(m)$. Similar to Eq. (47), we approximate $\delta\rho^{(\mathrm{b})}(m)$ by

$$\delta\rho^{(\mathrm{b})}(m) = S^\dagger(m)\,\delta\rho^{(\mathrm{a})}(m)\,S(m), \tag{48}$$

leading to the compact transformation rule

$$\rho^{\mathrm{red\,(b)}}(m) = S^\dagger(m)\,\rho^{\mathrm{red\,(a)}}(m)\,S(m). \tag{49}$$

The complementary transformation rule for switching from $\mathcal{H}^b$ to $\mathcal{H}^a$ reads

$$\rho^{\mathrm{red\,(a)}}(m) = S(m)\,\rho^{\mathrm{red\,(b)}}(m)\,S^\dagger(m). \tag{50}$$

It should be emphasized that Eq. (48) is an *ad hoc* approximation, whose quality is difficult to assess *a priori*. Its accuracy is necessarily controlled by the smallness of $\langle\delta\psi^{(\alpha)}|\delta\psi^{(\alpha)}\rangle$, which in turn is reduced the smaller is M. Below, we present numerical results demonstrating this point.

In addition to the reduced density matrix, Eq. (32) requires explicit knowledge of the projected state, either $|\chi^{(\mathrm{a})}_M(t)\rangle$ or $|\chi^{(\mathrm{b})}_M(t)\rangle$, depending on the time interval in question. It is therefore necessary to formulate the transformation rule of $|\chi_M(t)\rangle$ upon conversion of the Hamiltonian. Focusing again on the time instance $t = t_{2n}$, the state $|\chi^{(\mathrm{b})}_M(t_{2n})\rangle$ is formally given by

$$\begin{aligned}\big|\chi^{(\mathrm{b})}_M(t_{2n})\big\rangle &= \hat{1}^+_{b,M}|\psi(t_{2n})\rangle \\ &= \sum_{m=m_{\min}}^{M} \hat{1}^+_{b,M}\big|\phi^{(\mathrm{a})}_m(t_{2n})\big\rangle + \hat{1}^+_{b,M}\big|\chi^{(\mathrm{a})}_M(t_{2n})\big\rangle,\end{aligned} \tag{51}$$

where $|\phi^{(\mathrm{a})}_m(t_{2n})\rangle$ and $|\chi^{(\mathrm{a})}_M(t_{2n})\rangle$ are projected according to the operators $\hat{P}_{a,m}$ and $\hat{1}^+_{a,M}$ pertaining to the Hamiltonian $\mathcal{H}^a$. The right-most term in Eq. (51) has the exact representation

$$\hat{1}^+_{b,M}\big|\chi^{(\mathrm{a})}_M(t_{2n})\big\rangle = S^\dagger(M)\big|\chi^{(\mathrm{a})}_M(t_{2n})\big\rangle, \tag{52}$$

which follows from the fact that $\hat{P}_{a,m}|\chi^{(\mathrm{a})}_M(t_{2n})\rangle$ vanishes by construction for all $m \leqslant M$. As for the remaining terms on the right-hand side of Eq. (51), these require explicit knowledge of the states $|\phi^{(\mathrm{a})}_m(t_{2n})\rangle$. Unfortunately, it is unfeasible to keep track of the states $|\phi^{(\mathrm{a})}_m(t)\rangle$, which forces yet another approximation. Our strategy is to omit these terms altogether, with the expectation that their combined contribution is typically small. Naturally, the quality of this approximation will depend on the choice of M and on details of $\mathcal{H}^a$ and $\mathcal{H}^b$. This leaves us with the approximate transformation rule

$$\big|\chi^{(\mathrm{b})}_M(t_{2n})\big\rangle \approx S^\dagger(M)\big|\chi^{(\mathrm{a})}_M(t_{2n})\big\rangle, \tag{53}$$

along with its counterpart

$$\big|\chi^{(\mathrm{a})}_M(t_{2n+1})\big\rangle \approx S(M)\big|\chi^{(\mathrm{b})}_M(t_{2n+1})\big\rangle. \tag{54}$$

We are now in position to summarize the proposed algorithm for computing $A(t) = \langle\psi(t)|\hat{A}|\psi(t)\rangle$ for a sequence of switching events. We begin by rewriting Eq. (32) in the form

$$A(t) = \sum_{m=m_{\min}}^{M}\sum_{r,s}^{\mathrm{trun}} A^{m,(\alpha)}_{r,s}\rho^{\mathrm{red}\,(\alpha)}_{s,r}(m;t) + \big\langle\chi^{(\alpha)}_M(t)\big|\hat{A}\big|\chi^{(\alpha)}_M(t)\big\rangle, \tag{55}$$

where α equals a or b depending on the time interval, and $A^{m,(\alpha)}_{r,s}$ is the matrix representation of $\hat{A}$ at iteration m with respect to the NRG eigenstates of $\mathcal{H}^\alpha$. The first step is to evaluate $\rho^{\mathrm{red\,(a)}}_{s,r}(m;t=0)$ and $|\chi^{(\mathrm{a})}_M(t=0)\rangle$ using the TD-NRG methodology detailed in Ref. 31 and in Sec. II C 3 above. From this point on, these quantities are evolved in time according to the following set of rules: (i) at time $t = t_{2n}$ we switch from $\mathcal{H}^a$ to $\mathcal{H}^b$ by setting

$$\begin{aligned}\rho^{\mathrm{red\,(b)}}(m;t_{2n}) &= S^\dagger(m)\,\rho^{\mathrm{red\,(a)}}(m;t_{2n})\,S(m), \\ \big|\chi^{(\mathrm{b})}_M(t_{2n})\big\rangle &= S^\dagger(M)\big|\chi^{(\mathrm{a})}_M(t_{2n})\big\rangle.\end{aligned} \tag{56}$$

(ii) In the time interval $t_{2n} \leqslant t \leqslant t_{2n+1}$, the density matrices and wave function are propagated in time according to

$$\begin{aligned}\rho^{\mathrm{red\,(b)}}_{s,r}(m;t) &= \rho^{\mathrm{red\,(b)}}_{s,r}(m;t_{2n})\,e^{i(E^m_r - E^m_s)(t-t_{2n})}, \\ \big|\chi^{(\mathrm{b})}_M(t)\big\rangle &= e^{-i\hat{h}^b_\chi(t-t_{2n})}\big|\chi^{(\mathrm{b})}_M(t_{2n})\big\rangle,\end{aligned} \tag{57}$$

where $\hat{h}^b_\chi$ is the projected low-energy Hamiltonian corresponding to $\mathcal{H}^b$. (iii) At time $t = t_{2n+1}$, we switch back from $\mathcal{H}^b$ to $\mathcal{H}^a$ by setting

$$\begin{aligned}\rho^{\mathrm{red\,(a)}}(m;t_{2n+1}) &= S(m)\,\rho^{\mathrm{red\,(b)}}(m;t_{2n+1})\,S^\dagger(m), \\ \big|\chi^{(\mathrm{a})}_M(t_{2n+1})\big\rangle &= S(M)\big|\chi^{(\mathrm{b})}_M(t_{2n+1})\big\rangle.\end{aligned} \tag{58}$$

(iv) The density matrices and wave function are propagated in the time interval $t_{2n+1} \leqslant t \leqslant t_{2n+2}$ according to

$$\begin{aligned}\rho^{\mathrm{red\,(a)}}_{s,r}(m;t) &= \rho^{\mathrm{red\,(a)}}_{s,r}(m;t_{2n+1})\,e^{i(E^m_r - E^m_s)(t-t_{2n+1})}, \\ \big|\chi^{(\mathrm{a})}_M(t)\big\rangle &= e^{-i\hat{h}^a_\chi(t-t_{2n+1})}\big|\chi^{(\mathrm{a})}_M(t_{2n+1})\big\rangle,\end{aligned} \tag{59}$$

where $\hat{h}^a_\chi$ is the projected low-energy Hamiltonian corresponding to $\mathcal{H}^a$.

We stress that four distinct approximations enter Eqs. (56)–(59): (i) a discrete representation of the continuous bath, (ii) the standard NRG approximation $\mathcal{H}_N|r,e;m\rangle \approx E^m_r|r,e;m\rangle$ that is used to propagate the reduced density matrices within

each time interval where $\mathcal{H}$ is fixed, (iii) the transformation rule of Eq. (48) for $\delta\rho(m)$ at each switching event, and (iv) The omission of those terms that originate from the $|\phi_m\rangle$'s in Eq. (51) in the transformation rule for $|\chi_M(t)\rangle$ at each switching event. While the first two approximations are general in nature and apply, in particular, to the TD-NRG, the latter two approximations are specific to the present formulation of repeated switchings. The quality of those approximations, which become exact for $M = m_{\min}$, can be tested *a posteriori* by comparison to cases where exact solutions are available, as done in Sec. VI A for the noninteracting resonant-level model.

IV. CHEBYSHEV EXPANSION TECHNIQUE

Our presentation thus far was quite general and did not specify a particular method to be hybridized with the TD-NRG. As a proof of principle, we shall demonstrate in Sec. VI the hybridization of the TD-NRG with the CET, whose principles and implementation are reviewed below.

The CET[27–29] offers an accurate way to calculate the time evolution of an initial state $|\psi_0\rangle$ under the influence of a general stationary finite-dimensional Hamiltonian $\mathcal{H}$:

$$|\psi(t)\rangle = e^{-i\mathcal{H}t}|\psi_0\rangle. \tag{60}$$

The main idea of the method is to construct a stable numerical approximation for the time-evolution operator $e^{-i\mathcal{H}t}$ that is independent of the initial state $|\psi_0\rangle$ and whose error can be reduced to machine precision. Its limitation lies in the need to explicitly store certain states in the course of the calculation, which limits the size of the Hilbert space that can be handled.

There are different ways to expand the time-evolution operator, the most direct one being the conventional expansion of the exponent in powers of $\mathcal{H}$. One would like, however, to use an expansion that converges uniformly, independent of the initial state $|\psi_0\rangle$. A suitable choice are the Chebyshev polynomials, defined by the recursion relation

$$T_{n+1}(z) = 2zT_n(z) - T_{n-1}(z), \tag{61}$$

subject to the initial conditions $T_0(z) = 1$ and $T_1(z) = z$. As is well known, the Chebyshev polynomials can be used to expand any function $f(z)$ on the interval $-1 \leqslant z \leqslant 1$. Explicitly, $f(z)$ is expressed as an infinite series

$$f(z) = \sum_{n=0}^{\infty} b_n T_n(z), \tag{62}$$

where the expansion coefficients b_n are given by

$$b_n = \frac{2-\delta_{n,0}}{\pi}\int_{-1}^{1}\frac{f(x)T_n(x)}{\sqrt{1-x^2}}dx. \tag{63}$$

The expansion in terms of Chebyshev polynomials can be equally applied to any function $F(z)$ with an arbitrary support $\lambda_{\min} \leqslant z \leqslant \lambda_{\max}$ using the transformation

$$z' = 2\frac{z-\lambda_{\min}}{\lambda_{\max}-\lambda_{\min}} - 1, \tag{64}$$

which maps the interval $\lambda_{\min} \leqslant z \leqslant \lambda_{\max}$ onto $-1 \leqslant z' \leqslant 1$. In doing so, one expands in practice the function $f(z') = F(z)$.

Using the rules detailed above, the function e^{-iz} is expanded for $\lambda_{\min} \leqslant z \leqslant \lambda_{\max}$ as

$$e^{-iz} = \sum_{n=0}^{\infty} b_n T_n(z') \tag{65}$$

with

$$b_0 = e^{-i\varphi} J_0\left(\frac{\Delta\lambda}{2}\right), \tag{66a}$$

$$b_{n>0} = 2i^n e^{-i\varphi} J_n\left(\frac{\Delta\lambda}{2}\right). \tag{66b}$$

Here, $J_n(x)$ are the Bessel functions, φ equals $(\lambda_{\max}+\lambda_{\min})/2$, and $\Delta\lambda = \lambda_{\max} - \lambda_{\min}$. Accordingly, the time-evolution operator $e^{-i\mathcal{H}t}$ is expanded as

$$e^{-i\mathcal{H}t} = \sum_{n=0}^{\infty} b_n(t) T_n(\mathcal{H}'), \tag{67}$$

where

$$b_0(t) = e^{-i\alpha t} J_0\left(\frac{\Delta E t}{2}\right), \tag{68a}$$

$$b_{n>0}(t) = 2i^n e^{-i\alpha t} J_n\left(\frac{\Delta E t}{2}\right). \tag{68b}$$

Here, $E_{\max}$ ($E_{\min}$) is the maximal (minimal) eigenenergy of $\mathcal{H}$, ΔE equals $E_{\max} - E_{\min}$, $\alpha = (E_{\max}+E_{\min})/2$, and $\mathcal{H}'$ is the "transformed" Hamiltonian

$$\mathcal{H}' = 2\frac{\mathcal{H}-E_{\min}}{E_{\max}-E_{\min}} - 1. \tag{69}$$

Finally, applying Eq. (67) to the initial state $|\psi_0\rangle$, one obtains

$$|\psi(t)\rangle = \sum_{n=0}^{\infty} b_n(t)|\phi_n\rangle, \tag{70}$$

where the infinite set of states $|\phi_n\rangle = T_n(\mathcal{H}')|\psi_0\rangle$ obey the recursion relation[27]

$$|\phi_{n+1}\rangle = 2\mathcal{H}'|\phi_n\rangle - |\phi_{n-1}\rangle, \tag{71}$$

subject to the initial condition $|\phi_0\rangle = |\psi_0\rangle$ and $|\phi_1\rangle = \mathcal{H}'|\psi_0\rangle$.

Several comments are in order. First, all time dependence is confined in Eq. (70) to the expansion coefficients $b_n(t)$ of Eqs. (68), which are independent of the initial state $|\psi_0\rangle$. Second, the Chebyshev recursion relation of Eq. (71) reveals the iterative nature of the calculations. Starting form the initial state $|\psi_0\rangle$, one constructs all subsequent states $|\phi_n\rangle$ using repeated applications of the "transformed" Hamiltonian $\mathcal{H}'$. Note that in practice only two such states need be stored in memory at each given time. Third, since $J_n(x) \sim (ex/2n)^n$ for large order n, the Chebyshev expansion converges quickly as n exceeds $\Delta E t$. Finally, the Chebyshev expansion has the virtue that numerical errors are practically independent of t, allowing access to extremely long times. The main limitation of the approach, as commented above, stems from the size of the Hilbert space, since each of the states $|\phi_n\rangle$ must be constructed explicitly. In our applications of the approach (where $|\chi_M\rangle$ serves as the initial state), this Hilbert space comprises the tensor products of the kept NRG states at iteration M—typically of the order of 2^{10} states— and the

remaining chain $R_{M,N}$, whose dimension is d^{N-M} ($d = 2$ being the number of distinct configurations of a single spinless site). As a result, application of the CET is confined to rather short chains that cannot be used to access arbitrarily long time scales.

V. SINGLE-QUENCH DYNAMICS ON A HYBRID CHAIN

As already pointed out in the introduction, the Wilsonian discretization of the continuous bath significantly influences the quench dynamics, independent of which finite-size approach—exact diagonalization, TD-NRG, or the TD-DMRG—is used to track the real-time dynamics of the system. As illustrated in Fig. 1, deviations from the exact continuum-limit result stem from current reflections at sites along the Wilson chain, caused by the exponentially decreasing hopping matrix elements that are used. These in turn produce an exponentially decreasing transport velocity.

In this section, we present a preliminary discussion aimed at demonstrating the potential of substituting the standard Wilson chain with a hybrid chain of the type depicted in Fig. 4. We shall do so by investigating a single quantum quench in the noninteracting resonant-level model (RLM), which can be solved exactly on essentially any finite-size chain using exact diagonalization of the single-particle eigenmodes. The availability of an exact analytical solution for the real-time dynamics of the level occupancy in the continuum limit [see Eq. (50) of Ref. 31] makes this model an ideal benchmark for testing the quality of different hybrid chains in reproducing the continuum-limit result. Thus one can clearly separate deviations caused by the structure of the chain from those that originate from further approximations underlying the TD-DMRG or TD-NRG. Furthermore, the RLM sets the stage for more complicated interacting models, such as the interacting resonant-level model discussed below.

Physically, the RLM describes the coupling of a single spinless level to a continuous band of width 2D via the single-particle hopping matrix element V:

$$\mathcal{H} = \sum_k \epsilon_k c_k^\dagger c_k + E_d d^\dagger d + \frac{V}{\sqrt{N_k}} \sum_k (c_k^\dagger d + \text{H.c.}). \qquad (72)$$

Here, $d^\dagger$ creates an electron on the level, $c_k^\dagger$ creates a band electron with momentum k, and N_k labels the number of distinct values of k. The relevant energy scales in the problem include the level energy E_d, along with the hybridization width $\Gamma_0 = \pi \varrho V^2$, where ϱ is the conduction-electron density of states at the Fermi level.

We are interested in tracking the real-time dynamics of the level occupancy $n_d(t) = \langle d^\dagger(t) d(t) \rangle$ in response to a sudden quench from (E_d^i, Γ_i) to (E_d^f, Γ_f). Figure 5 depicts the time evolution of $n_d(t)$ after the level energy has been abruptly shifted from $E_d^i = -2\Gamma_0$ to $E_d^f = 2\Gamma_0$ while keeping the hybridization width fixed at Γ_0. We used the same model parameters as in Fig. 1, but varied the chain structure by considering different values of the partitioning parameter M and different chain lengths N. Explicitly, as illustrated in Fig. 4, these chains comprise an initial Wilson chain with exponentially decreasing hopping matrix elements $t_m \propto \Lambda^{-m/2}$ up to $m = M$, converting to a constant hopping matrix element $t_m = t_M$ for $M \leqslant m \leqslant N$.

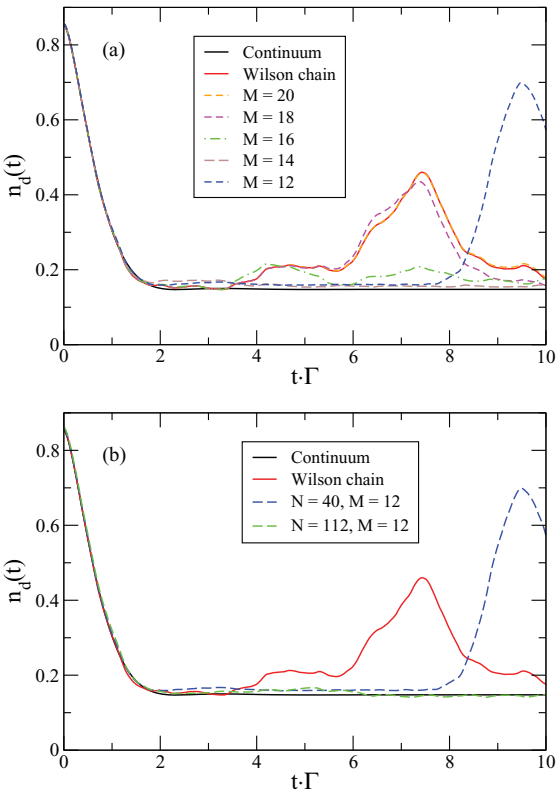

FIG. 5. (Color online) Comparison of the exact continuum-limit solution for $n_d(t)$ in the RLM (solid black line) and its exact numerical evaluation for various hybrid chains of the type depicted in Fig. 4. The full red line depicts the case of a pure Wilson chain of length $N = 40$. (a) Keeping the total chain length fixed at $N = 40$ and varying the partitioning parameter M. (b) For $M = 12$ and two different chain lengths $N = 40$ and 112. Model parameters are $\Gamma_i = \Gamma_f = \Gamma_0$, $E_d^f = -E_d^i = 2\Gamma_0$, $\Gamma_0/D = 10^{-2}$, and $\Lambda = 1.8$.

As can be seen in Fig. 5(a), there is a systematic improvement in the agreement with the continuum-limit result upon decreasing M. Specifically, for $M = 12$, the deviations remain quite small up to $t\,\Gamma \sim 8$, at which point, there is a revival of $n_d(t)$, which nearly reaches its original value $n_d(t = 0)$ for $t\,\Gamma \approx 9.5$. In contrast to a pure Wilson chain, the current velocity becomes a constant along the chain sites with $m > M$, hence current reflections occur only at the end of the chain.[22] The time at which the revival of $n_d(t)$ is observed is simply given by the round-trip time for a charge pulse that originates from the impurity to reach the chain end and return. Note that this time is shorter for $M = 12$ than for $M = 14$.

Since charge is a globally conserved quantity, true thermalization and relaxation can occur only in the thermodynamic limit $N \to \infty$. The deviation of the total charge from its thermalized value following the quench is simply given by the difference in the equilibrated charges before and after the quench. Since the change in total charge is $\mathcal{O}(1)$ for such a local quench, there is an $\mathcal{O}(1/N)$ contribution to each reservoir degree of freedom, which can be safely neglected in the thermodynamic limit.

For any finite-size chain, however, this effect remains finite and relevant for the long-time limit. In particular, the continuity equation leads to charge reflections at the end of the tight-binding chain[22,37] such that the round-trip time is controlled by the chain length. Indeed, in Fig. 5(b), we compare $n_d(t)$ for two hybrid chains, each partitioned at $M = 12$. The two chains share the same characteristic energy scale D_M for their partitioning, but one has a total length of $N = 40$ and the other $N = 112$. While the short-time dynamics is nearly identical and agrees well with the continuum-limit result, the revival time for the long hybrid chain is pushed way beyond the time interval presented in Fig. 5. Thus discretization errors have been nearly eliminated on the time scale of interest.

This latter example vividly illustrates the potential of hybridizing the TD-NRG with the TD-DMRG, as the tight-binding chain length involved is of typical DMRG size. Since in our example the effective bandwidth D_M is of order Γ_0, the TD-NRG generates an effective Hamiltonian h_χ whose effective bandwidth D_M can be of several orders of magnitude smaller than the bare conduction-electron bandwidth D. This in turn allows access to long-time scales of order $1/\Gamma_0 \gg 1/D$, which lie beyond the reach of pure TD-DMRG, while significantly reducing discretization errors that are inherent to the TD-NRG.

A concluding word is in order about the optimal choices of M and the structure of the hybrid chain. The answers to these questions are quite difficult and can be expected to depend both on the model and observable of interest. For instance, spin and charge excitations generally propagate with different velocities. It is therefore quite feasible that the optimal choices of M and N will dependent on the observable in question. A more systematic study of the optimal hybrid chain is left for future research.

VI. PERIODIC SWITCHING

A. Periodic switching in the resonant-level model

So far, we have stressed the potential of using hybrid chains by comparing their exact numerical solutions with the continuum-limit result for simple quenches. In this section, we extend our focus to the hybrid-NRG approach as formulated in Sec. III for periodic switching. To benchmark our switching algorithm, we compare it with exact diagonalization solutions on a pure Wilson chain, postponing further discussion of the usage of hybrid chains and the comparison to exact continuum-limit results. Therefore all calculations are performed on a standard Wilson chain with identical parameters, hybridizing the CET with the TD-NRG at a given site M. In order to illustrate how the effective low-energy Hamiltonian generated by the NRG can be fed into the CET (or into any other method of choice for that matter), we consider an extreme wide-band limit by setting the bare bandwidth of the RLM to $D = 10^5\Gamma_0$.

Using the notations introduced in Sec. III, we start at time $t = 0$ with a system that resides in the ground state of $\mathcal{H}^a$, and switch repeatedly between $\mathcal{H}^a$ and $\mathcal{H}^b$ after each additional time interval τ. As our basic energy scale, we set $\Gamma_0 = 10^{-5}D$, whose associated time scale $1/\Gamma_0 = 10^5/D$ lies many orders of magnitude beyond the reach of the CET when applied directly to the full Wilson chain. We work with a chain of fixed length $N = 84$ and the logarithmic discretization parameter $\Lambda = 1.4$, such that $D_N \sim \Gamma_0/10$.

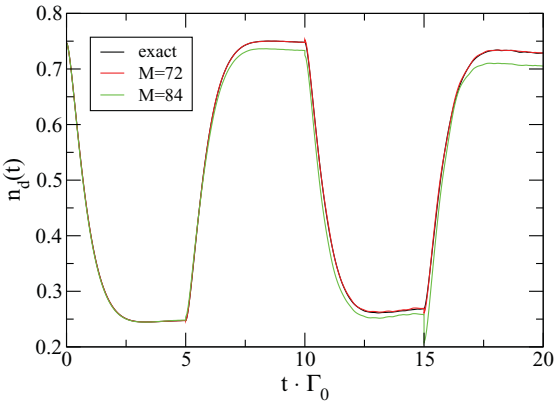

FIG. 6. (Color online) Comparison of the hybrid NRG-CET approach and exact diagonalization for the RLM on a Wilson chain with $\Lambda = 1.4$ and $N = 84$. The TD-NRG resummation is applied up to iteration M, beyond which the CET is used to track the time evolution of $|\chi_M(t)\rangle$. The number of states retained in the course of the NRG is equal to $N_s = 1024$. The resulting occupancy $n_d(t)$ is averaged over $N_z = 8$ equally distributed values of the twist parameter z, both for the hybrid-NRG and in exact diagonalization. Model parameters are $\Gamma_a = \Gamma_b = \Gamma_0$, $E_d^b = -E_d^a = \Gamma_0$, and $\tau = 5/\Gamma_0$, with $\Gamma_0/D = 10^{-5}$. Upon decreasing M, the hybrid NRG-CET approach gradually converges onto the exact result.

To initiate the calculation, we first perform an NRG run for the initial Hamiltonian $\mathcal{H}^a$ and select the ground state of the Nth iteration as our initial state[49] $|\psi_0\rangle$ (for even N the ground state is unique). We then perform a second NRG run for the other Hamiltonian $\mathcal{H}^b$, during which we construct the overlap matrices $S(m)$. Technically, these two NRG runs can be performed in parallel, in which case the overlap matrices $S(m)$ are calculated at the end of each NRG iteration. Backtracking from iteration N to iteration $m_{\min}$, the reduced density matrices $\rho^{\mathrm{red\,(a)}}(m;0)$ are computed using the standard TD-NRG algorithm.[31] These density matrices, along with the projected state $|\chi_M^{(a)}(0)\rangle$, are then used as a seed for the hybrid-NRG algorithm detailed in Eqs. (55)–(59).

1. Simple extension of the TD-NRG to periodic switching

Before discussing the full hybrid approach, let us focus for a moment on a simple extension of the TD-NRG to periodic switching, corresponding to setting $M = N$ in Eqs. (55)–(59). This implies taking $|\chi_M(t)\rangle = 0$ throughout the calculation.

Using $\tau = 5/\Gamma_0$ and $E_d^b = -E_d^a = \Gamma_0$, Fig. 6 depicts a comparison of the TD-NRG with an exact diagonalization solution on a Wilson chain with $N = M = 84$. Since the decay rate is given by Γ_0, the system almost fully equilibrates before the next switching event takes place. As a result the deviations of the periodic TD-NRG from the exact numerical solution are surprisingly small. In particular, the periodic TD-NRG correctly tracks the general structure of the precise solution. Nevertheless, a systematic degradation in accuracy is observed upon going from one switching cycle to the next. This loss of accuracy can be quantified by the growing discontinuity

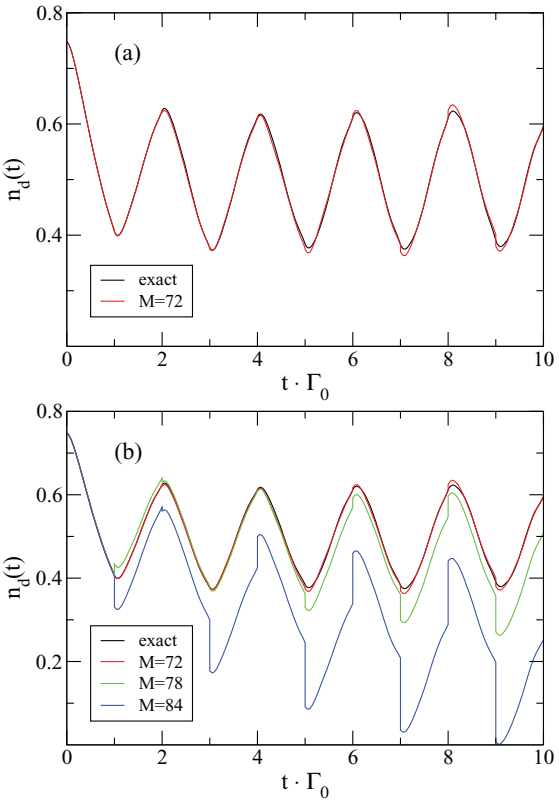

FIG. 7. (Color online) Same as Fig. 6 but for $\tau = 1/\Gamma_0$ and $N_z = 1$ (i.e., no z averaging). Note the much stronger M dependence as compared to $\tau = 5/\Gamma_0$.

$\Delta n_d^{(i)} = |n_d(t_i + 0^+) - n_d(t_i - 0^+)|$ at successive switching events, caused by the approximation made to $\rho^{\mathrm{red}\,(\alpha)}(m;t)$.

Reduction of the switching time to $\tau = 1/\Gamma_0$ prevents the system from relaxing to a new equilibrium state. In this case, high-energy excitations, which are cut off by neglecting the three additional terms $\delta\rho^{+-}(m)$, $\delta\rho^{-+}(m)$, and $\delta\rho^{--}(m)$, contribute significantly to the time evolution of $\hat{\rho}(t)$. Since switching occurs on a shorter time scale, energy is frequently pumped into the system, exciting it in such a way that the three neglected high-energy contributions to $\rho^{\mathrm{red}\,(\alpha)}(m;t)$ gain increasing importance with time. Indeed, the periodic TD-NRG result for $n_d(t)$, depicted by the blue curve in Fig. 7(b), shows a sizable accumulated error that grows systematically in time.

2. *Hybrid approach to periodic switching*

Although the simple periodic extension of the TD-NRG already captures the correct short-time dynamics, the externally driven nonequilibrium state increasingly deviates with time from the transient dynamics of a single quantum quench. Energy is locally added and removed from the system, which can be partially dissipated via heat current flowing between the impurity and the finite-size bath.

To properly capture this physics, we next employ the hybrid approach to periodic switching. The key idea is to identify a suitable low-energy subspace that is large enough for the neglected contributions in our approximation to be small. A trivial limit is given by setting $M \leqslant m_{\mathrm{min}}$, for which the hybrid approach reproduces by construction the exact solution on the finite-size chain. Even though this limit has no practical value, it illustrates the point that a reduction in M should systematically improve the quality of the results.

With this understanding, we extend our discussion of the hybrid approach to $m_{\mathrm{min}} < M < N$. At each time interval where $\mathcal{H}$ is fixed we evolve $|\chi_M^{(\alpha)}(t)\rangle$ in time using the CET, which is essentially exact on all time scales of interest. The CET is restricted, however, in the size of the Hilbert space one can treat, which limits the length of the residual chain $R_{M,N}$ extending beyond site M. With our machines we can comfortably access up to $2^{22} \approx 4 \times 10^6$ basis states, above which the computational effort rapidly becomes too exhaustive. Keeping $N_s = 2^{10} = 1024$ states at the conclusion of each NRG iteration, this sets an upper limit of 12 addition Wilson sites beyond site M, i.e., $M \geqslant N - 12 = 72$. To reduce finite-size effects, we average over N_z equally distributed values of the twist parameter[50] $z \in (0,1]$. Below, we present results for different values of $M \geqslant 72$ and $N_z \geqslant 1$.

Figures 6 and 7 show the time evolution of $n_d(t)$ in response to repeated switchings between $E_d^a = -\Gamma_0$ and $E_d^b = \Gamma_0$, keeping $\Gamma_a = \Gamma_b = \Gamma_0$ fixed. Figure 6 depicts four successive switch events with the time interval $\tau = 5/\Gamma_0$, while Fig. 7 shows ten successive switch events with the shorter time interval $\tau = 1/\Gamma_0$. For comparison, the exact time evolutions on the Wilson chain are depicted by the black lines, after averaging over the different values of z. These solutions are obtained by exact diagonalization of the single-particle eigenmodes of each Hamiltonian and using them to propagate $d^\dagger(t)d(t)$ in time.

Several points are noteworthy. Upon decreasing M, the hybrid NRG-CET curves gradually converge onto the exact result for the Wilson chain, both for $\tau = 1/\Gamma_0$ and $\tau = 5/\Gamma_0$. Specifically, by $M = 72$ the hybrid NRG-CET approach essentially reproduces the exact curves. The largest deviations are usually found immediately following a switching event, when a discontinuity generally develops in the occupancy produced by the hybrid NRG-CET approach. As noted above, the discontinuity stems from the approximations employed in deriving Eqs. (56)–(59). It decreases in size with decreasing M, reflecting a reduction in the accumulated weight of the $|\phi_m(t)\rangle$'s in favor of $|\chi_M(t)\rangle$ in the expansion of Eq. (14). Indeed, the smaller the accumulated weight of the $|\phi_m(t)\rangle$'s the more accurate are the approximations employed in deriving the hybrid-NRG.

For $M = 84$, the hybrid approach corresponds to the simple extension of the TD-NRG to periodic switching. As can be seen in Fig. 7(b), the discontinuities at $t_n = n\tau$ are particularly large for the shorter switching time $\tau = 1/\Gamma_0$ since more energy is pumped into the system. These discontinuities are greatly reduced for the longer time interval $\tau = 5/\Gamma_0$ as depicted in Fig. 6. As discussed above, this behavior is correlated with the fact that the occupancy $n_d(t)$ for $\tau = 5/\Gamma_0$ has nearly decayed in each time interval to its new equilibrium value corresponding to the Hamiltonian $\mathcal{H}^\alpha$ in that time segment. In other terms, the state of the system behaves as if it has effectively decayed to the new ground state, leaving behind only weak traces of the transient behavior.

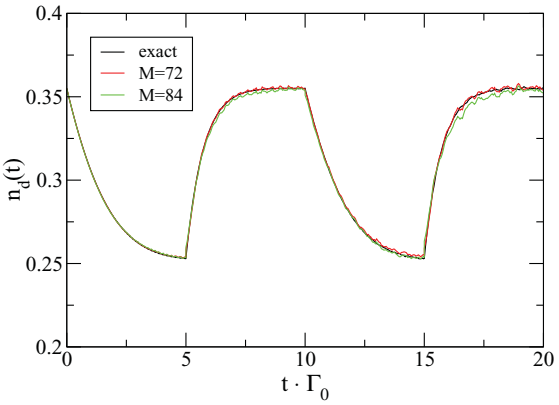

FIG. 8. (Color online) The time-dependent response to repeated switchings between $\Gamma_a = \Gamma_0/2$ and $\Gamma_b = \Gamma_0$ for fixed $E_d^a = E_d^b = \Gamma_0/2$. All other parameters are the same as in Fig. 6.

Figure 8 shows the complementary response to repeated switchings between two different hybridization widths: $\Gamma_a = \Gamma_0/2$ and $\Gamma_b = \Gamma_0$ for fixed $E_d^a = E_d^b = \Gamma_0/2$. As can be seen, the discontinuities at $t_n = n\tau$ are barely visible in this case, yet discretization errors do give rise to high-frequency wiggles that are essentially absent in Figs. 6 and 7. The usage of z averaging is essential for reducing these discretization effects, both at the level of the hybrid-NRG and in the framework of exact diagonalization. Similar to the case of a single quantum quench, discretization errors become more and more pronounced the larger are the deviations between $\mathcal{H}^a$ and $\mathcal{H}^b$ and the longer the time that has elapsed. Clearly, the nature of the perturbation (e.g., $E_d^a \neq E_d^b$ versus $\Gamma_a \neq \Gamma_b$) is also of importance. It should be emphasized, however, that z averaging alone is insufficient for removing low-frequency oscillations that appear when the deviations between $\mathcal{H}^a$ and $\mathcal{H}^b$ are large.

To summarize this section, we have demonstrated how the NRG can be used to systematically construct effective low-energy Hamiltonians $\hat{h}_\chi^a$ and $\hat{h}_\chi^b$ whose bandwidth is smaller by orders of magnitude than the bare conduction-electron bandwidth D of the original model. As a result, methods such as the TD-DMRG, whose accuracy is usually confined to times of order $10^2/D$, can be used within the hybrid platform to access exponentially long time scales. This follows from the fact that the new effective bandwidth $\approx D_M \propto D\Lambda^{-M/2}$ can be exponentially smaller than D.

B. Interacting resonant-level model

Having established the accuracy of the hybrid NRG-CET approach for the noninteracting RLM, we proceed to apply it to an interacting problem that lacks an exact reference solution. Specifically, we shall use the hybrid NRG-CET to track the real-time dynamics of the interacting resonant-level model (IRLM) in a regime not accessible to other available methods. In the IRLM,[39,40,42,43] the resonant-level model of Eq. (72) is supplemented by a local contact interaction U between the level and the band electrons:

$$\mathcal{H}_U = U\left(d^\dagger d - \frac{1}{2}\right)\frac{1}{N_k}\sum_{k,k'} :c_k^\dagger c_{k'}:. \tag{73}$$

Here $:c_k^\dagger c_{k'}: = c_k^\dagger c_{k'} - \delta_{k,k'}\theta(-\epsilon_k)$ stands for normal ordering with respect to the filled Fermi sea. Physically, the contact interaction U accounts for the local capacitive coupling between the localized level $d^\dagger$ and the band electrons. The total Hamiltonian of the model is given by

$$\mathcal{H} = \mathcal{H}_{\rm RLM} + \mathcal{H}_U, \tag{74}$$

where $\mathcal{H}_{\rm RLM}$ represents the RLM Hamiltonian of Eq. (72).

At low energies, the IRLM is equivalent to a renormalized noninteracting RLM, both describing a phase-shifted Fermi liquid.[41,51] At resonance, the model is characterized by the renormalized tunneling rate

$$\Gamma_{\rm eff} \approx D\left(\frac{\Gamma_0}{D}\right)^{1/(1+\alpha)}, \tag{75}$$

where $\Gamma_0 = \pi\varrho V^2$ is the noninteracting hybridization width of the RLM defined in Eq. (72), α equals $2\tilde{\delta} - \tilde{\delta}^2$, and

$$\tilde{\delta} = (2/\pi)\arctan(\pi\varrho U/2) \tag{76}$$

is the scattering phase shift associated with U alone (namely, in the absence of V). Within the NRG, $\Gamma_{\rm eff}$ is conveniently extracted from the zero-temperature charge susceptibility $\chi_c = -dn_d/dE_d$, evaluated at $E_d = 0$. Explicitly, we adopt the working definition $\Gamma_{\rm eff} = 1/(\pi\chi_c)$.

In Fig. 9, we show the time evolution of $n_d(t)$ in response to repeated switchings between $E_d^a = -\Gamma_{\rm eff}$ and $E_d^b = \Gamma_{\rm eff}$ for $U/D = 1$. The bare hybridization strength $\Gamma_a = \Gamma_b = \Gamma_0 = 6 \times 10^{-9} D$ was adjusted numerically so as to maintain a fixed $\Gamma_{\rm eff} = 10^{-5} D$. The effect of a finite U is twofold. First, it renormalizes the bare hybridization width from Γ_0 to $\Gamma_{\rm eff}$, which sets the basic time scale in the problem: $1/\Gamma_{\rm eff}$. Second, there are pronounced oscillations that are absent for $U = 0$, having the characteristic period $t_{\rm osc} \approx 3/\Gamma_{\rm eff}$. To illustrate this point, we have borrowed from Fig. 6 the exact time evolution of $n_d(t)$ on the Wilson chain for $U = 0$ and $\Gamma_a = \Gamma_b = \Gamma_0 = 10^{-5} D$. The effect of U clearly goes beyond just a simple renormalization of the parameters of the noninteracting RLM, generating new interaction-induced oscillations.

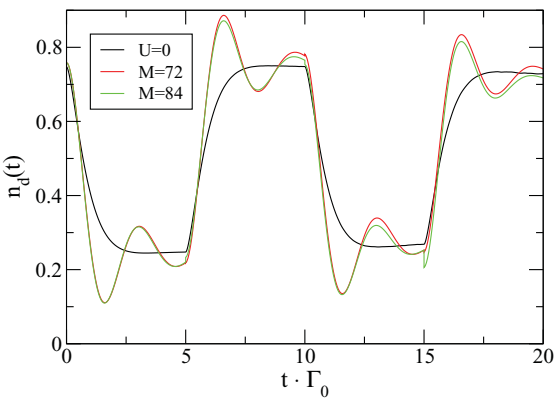

FIG. 9. (Color online) Same as Fig. 6, for $U/D = 1$ and $E_d^b = -E_d^a = \Gamma_{\rm eff}$. Here, $\Gamma_a = \Gamma_b = \Gamma_0 = 6 \times 10^{-9} D$ was adjusted so as to maintain a fixed $\Gamma_{\rm eff} = 10^{-5} D$. The black line shows for comparison the exact time evolution on the Wilson chain for $U = 0$ and $\Gamma_a = \Gamma_b = \Gamma_0 = 10^{-5} D$ (taken from Fig. 6).

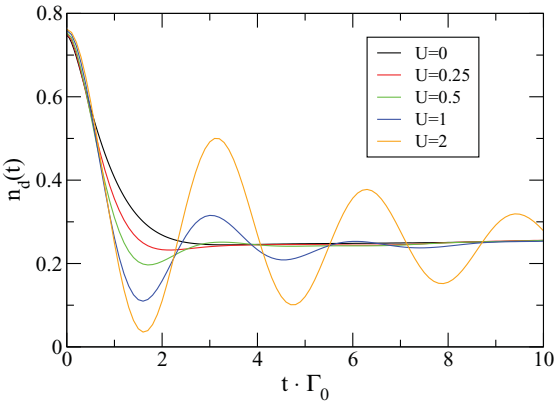

FIG. 10. (Color online) The real-time dynamics following a single quantum quench from $E_d^a = -\Gamma_{\rm eff}$ to $E_d^b = \Gamma_{\rm eff}$, for the IRLM with $\Gamma_a = \Gamma_b = \Gamma_0$ and different values of the Coulomb repulsion U. Here, Γ_0 was adjusted separately for each value of U so as to maintain a fixed $\Gamma_{\rm eff} = 10^{-5}D$. All remaining parameters are as in Fig. 6.

To further investigate this point, we have plotted in Fig. 10 the real-time dynamics in response to a single quantum quench from $E_d^a = -\Gamma_{\rm eff}$ to $E_d^b = \Gamma_{\rm eff}$, for different values of the Coulomb repulsion U. The bare hybridization width $\Gamma_a = \Gamma_b = \Gamma_0$ was adjusted separately for each value of U so as to maintain a fixed $\Gamma_{\rm eff} = 10^{-5}D$. All curves begin at essentially the same initial occupancy $n_d \simeq 0.75$ and decay at long time to $n_d \simeq 0.25$. Hence the low-energy fixed point, which governs the thermodynamics, is fully determined by $\Gamma_{\rm eff}$ and E_d.

The intermediate dynamics, on the other hand, is quite sensitive to U. Starting from $U = 0$ and increasing U, damped oscillations gradually develop with a characteristic period that only weakly depends on U. In contrast, the amplitude of the oscillations and their damping rate strongly depend on U. The larger is U, the slower does the envelope function decay to zero, resulting in the emergence of two distinct time scales for large U: the period of oscillations $t_{\rm osc}$ and the characteristic damping time $t_{\rm damp}$. For example, while $t_{\rm osc} \simeq 3.1/\Gamma_{\rm eff}$ for $U/D = 2$, the corresponding damping time is of order $10/\Gamma_{\rm eff}$.

To understand the origin of these interaction-induced oscillations, it is instructive to consider the limit of a large Coulomb repulsion, $U \to \infty$. In this extreme, the level degree of freedom $d^\dagger$ and the zeroth Wilson shell $f_0^\dagger$ decouple from the rest of the chain, being confined to a total valence of one: $d^\dagger d + f_0^\dagger f_0 = 1$ [this valence is fixed by the normal-ordered form of $\mathcal{H}_U$ as defined in Eq. (73)]. The corresponding subspace comprises the two configurations $d^\dagger|0\rangle$ and $f_0^\dagger|0\rangle$, where $|0\rangle$ denotes the state in which the resonant level and the zeroth Wilson shell are both empty. Omitting the coupling to the rest of the chain, the problem has been reduced in effect to a 2×2 matrix whose eigenenergies are

$$\epsilon_\pm = \frac{E_d}{2} \pm \sqrt{\left(\frac{E_d}{2}\right)^2 + V^2}. \tag{77}$$

Consequently, $n_d(t)$ must display quantum beats with the frequency

$$\Omega = \epsilon_+ - \epsilon_- = 2\sqrt{\left(\frac{E_d}{2}\right)^2 + V^2}. \tag{78}$$

To make contact with Fig. 10, it is necessary to express the period $t_{\rm osc} = 2\pi/\Omega$ in terms of $\Gamma_{\rm eff} = 1/(\pi\chi_c)$. A straightforward calculation gives

$$n_d(E_d) = \frac{1}{2} - \frac{1}{4}\frac{E_d}{\sqrt{(E_d/2)^2 + V^2}}, \tag{79}$$

resulting in $\Gamma_{\rm eff} = 4V/\pi$. Substituting $V = (\pi/4)\Gamma_{\rm eff}$ into Eq. (78) then yields

$$t_{\rm osc} = \frac{4}{\Gamma_{\rm eff}}\frac{1}{\sqrt{1 + (2E_d/\pi\Gamma_{\rm eff})^2}}. \tag{80}$$

Finally, setting $E_d = \Gamma_{\rm eff}$ to match the value used in the curves of Fig. 10, one obtains $t_{\rm osc} = 3.37/\Gamma_{\rm eff}$, in excellent agreement with the period observed in Fig. 10.

Our strong-coupling analysis clearly reveals that U enters the quantum-beat frequency only via $\Gamma_{\rm eff}$. However, U directly influences the amplitude of the oscillations and their damping rate. In contrast to the period of oscillations, which is well described by $U \to \infty$, the damping time $t_{\rm damp}$ requires a finite coupling to the rest of the chain. For $U \to \infty$, the impurity and the zeroth Wilson shell decouple from the rest of the chain, resulting in coherent quantum beats between the two singly occupied eigenstates. Once U becomes finite the system can decay incoherently to the lowest of the two singly occupied states through a residual coupling to the rest of the chain. It is this decay that determines $t_{\rm damp}$. Since the residual coupling should scale as $1/U$ for large interactions, $t_{\rm damp}$ should scale as U^2 for $U \gg D$. This corresponds to a damping rate that falls off as $1/U^2$.

VII. DISCUSSION AND OUTLOOK

In this paper, we have extended the TD-NRG in two ways. First, we devised a platform for combining the TD-NRG with complementary methods such as the TD-DMRG and CET for tracking the real-time dynamics of quantum-impurity systems. Second, we extended the TD-NRG from its original realm of a single quantum quench to more complicated forms of driven dynamics where repeated switchings are applied to the system. As a proof of principle, we combined the TD-NRG with the CET to compute the response of a resonant level, both with and without interactions, to repeated switchings of its energy level and tunneling amplitude to the band. Such a model can be used to describe a single Coulomb-blockade resonance in small quantum dots in regimes where spin degeneracy is unimportant.

In the absence of interactions, we have critically examined our new approach by detailed comparisons to an exact evaluation of the time evolution on the Wilson chain. As long as the perturbations are not too large, good accuracy is maintained over a fairly large number of switching events. Usage of the hybrid NRG-CET greatly improves the accuracy in cases where large deviations develop between the exact curve and the one produced without invoking the CET, see, e.g., Fig. 7. Our

present implementation of the hybrid approach is subject to the inherent restriction of the CET to rather small finite-size systems. We expect a significant boost in accuracy and flexibility by combining the TD-NRG with the TD-DMRG, which is capable of treating far larger systems. In particular, our approach opens the possibility to boost the TD-DMRG to exponentially long time scales by using the TD-NRG to (i) construct an effective low-energy Hamiltonian and (ii) account for the short-time dynamics. This portion of the research is left for future work.

The potential of the hybrid approach was next demonstrated by applying it to repeated switchings in the IRLM. Apart from specially tuned models,[52] this constitutes to our knowledge the first study of such driven dynamics in interacting quantum impurity systems. Although equivalent at sufficiently low energies to a noninteracting RLM, the driven dynamics of the IRLM shows clear traces of the interaction. In particular, interaction-induced oscillations develop for strong Coulomb repulsion, which have no equivalent in the absence of interactions. We were able to explain the period of oscillations and its weak dependence on U by invoking the limit $U \to \infty$. The associated damping time scales as U^2, and can greatly exceed the natural damping time $1/\Gamma_0$ of the noninteracting RLM. Such a long damping time is strictly the effect of interactions.

ACKNOWLEDGMENTS

We are grateful to Dotan Goberman, Achim Rosch, Sebastian Schmitt, and Matthias Vojta for helpful discussions. This work was supported by the German-Israeli Foundation through Grant No. 1035-36.14, by the Israel Science Foundation through Grant No. 1524/07 (E.E. and A.S.), and by the Deutsche Forschungsgemeinschaft under AN 275/6-2 (F.G. and F.B.A).

[1] M. Greiner, O. Mandel, T. W. Hänsch, and I. Bloch, Nature (London) **51**, 419 (2002).
[2] T. Kinoshita, T. Wenger, and D. S. Weiss, Nature (London) **440**, 900 (2006).
[3] U. Weiss, *Quantum Dissipative Systems* (World Scientific, Singapure, 1999).
[4] J. M. Elzerman, R. Hanson, L. H. W. van Beveeren, B. Witkamp, L. M. K. Vandersypen, and L. P. Kouvenhoven, Nature (London) **430**, 431 (2004).
[5] J. R. Petta, A. C. Johnson, J. M. Taylor, E. A. Laird, A. Yacoby, M. D. Lukin, C. M. Marcus, M. P. Hanson, and A. C. Gossard, Science **309**, 2180 (2005).
[6] T. Chakraboty, *Charge Migration in DNA: Perspectives from Physics, Chemistry* (Springer, New York, 2007).
[7] D. Loss and D. P. DiVincenzo, Phys. Rev. A **57**, 120 (1998).
[8] M. A. Kastner, Rev. Mod. Phys. **64**, 849 (1992).
[9] H. Haug and A.-P. Jauho, *Quantum Kinetics in Transport and Optics of Semiconductors*, Springer Series in Solid-State Science Vol. 123 (Springer, Berlin, Berlin, Heidelberg, 1996).
[10] L. P. Kadanoff and G. Baym, *Quantum Statistical Mechanics* (Benjamin, New York, 1962).
[11] L. V. Keldysh, Sov. Phys. JETP **20**, 1018 (1965).
[12] H. Haug and S. W. Koch, *Quantum Theory of the optical and Electronic Properties of Semiconductors* (World Scientific, Singapore, 2004).
[13] D. C. Langreth and J. W. Wilkins, Phys. Rev. B **6**, 3189 (1972).
[14] D. Goldhaber-Gordon, H. Shtrikman, D. Mahalu, D. Abusch-Magder, U. Meirav, and M. Kastner, Nature (London) **391**, 156 (1998).
[15] S. Schmitt and F. B. Anders, Phys. Rev. B **81**, 165106 (2010).
[16] K. G. Wilson, Rev. Mod. Phys. **47**, 773 (1975); R. Bulla, T. A. Costi, and T. Pruschke, *ibid*. **80**, 395 (2008).
[17] H. Schoeller, Eur. Phys. J. Special Topics **168**, 179 (2009).
[18] M. A. Cazalilla and J. B. Marston, Phys. Rev. Lett. **88**, 256403 (2002).
[19] H. G. Luo, T. Xiang, and X. Q. Wang, Phys. Rev. Lett. **91**, 049701 (2003).
[20] A. J. Daley, C. Kollath, U. Schollwöck, and G. Vidal, J. Stat. Mech.: Theor. Exp. (2004) P04005; D. Gobert, C. Kollath, U. Schollwoeck, and G. Schuetz, Phys. Rev. E **71**, 036102 (2005); U. Schollwöck, Rev. Mod. Phys. **77**, 259 (2005).
[21] S. R. White and A. E. Feiguin, Phys. Rev. Lett. **93**, 076401 (2004).
[22] P. Schmitteckert, Phys. Rev. B **70**, 121302(R) (2004); A. Branschaedel, G. Schneider, and P. Schmitteckert, Ann. Phys. **522**, 657 (2010).
[23] L. Mühlbacher and E. Rabani, Phys. Rev. Lett. **100**, 176403 (2008).
[24] P. Werner, T. Oka, and A. J. Millis, Phys. Rev. B **79**, 035320 (2009); P. Werner, T. Oka, M. Eckstein, and A. J. Millis, *ibid*. **81**, 035108 (2010).
[25] S. Weiss, J. Eckel, M. Thorwart, and R. Egger, Phys. Rev. B **77**, 195316 (2008).
[26] M. Schiró and M. Fabrizio, Phys. Rev. B **79**, 153302 (2009).
[27] A. Weiße, G. Wellein, A. Alvermann, and H. Fehske, Rev. Mod. Phys. **78**, 275 (2006).
[28] H. Tal Ezer and R. Kosloff, J. Chem. Phys. **81**, 3967 (1984).
[29] R. Kosloff, Annu. Rev. Phys. Chem. **45**, 145 (1994).
[30] F. B. Anders and A. Schiller, Phys. Rev. Lett. **95**, 196801 (2005).
[31] F. B. Anders and A. Schiller, Phys. Rev. B **74**, 245113 (2006).
[32] F. B. Anders, Phys. Rev. Lett. **101**, 066804 (2008); J. Phys. Condens. Matter **20**, 195216 (2008).
[33] A. C. Hewson, J. Phys. Condens. Matter **13**, 10011 (2001); A. C. Hewson, J. Bauer, and W. Koller, Phys. Rev. B **73**, 045117 (2006).
[34] D. C. Langreth and P. Nordlander, Phys. Rev. B **43**, 2541 (1991).
[35] H. Shao, D. C. Langreth, and P. Nordlander, Phys. Rev. B **49**, 13929 (1994).
[36] A. C. Hewson, J. Bauer, and A. Oguri, J. Phys. Condens. Matter **17**, 5413 (2005).
[37] P. Schmitteckert, J. Phys.: Conference Series **220**, 012022 (2010).
[38] A related objection has recently been raised by A. Rosch, who noted that the Wilson chain cannot serve as a proper heat reservoir even if made infinitely long; see the report e-print arXiv:1110.6514 (unpublished).
[39] P. Schlottmann, Phys. Rev. B **22**, 613 (1980).
[40] P. Mehta and N. Andrei, Phys. Rev. Lett. **96**, 216802 (2006).
[41] L. Borda, A. Schiller, and A. Zawadowski, Phys. Rev. B **78**, 201301 (2008).

[42]E. Boulat, H. Saleur, and P. Schmitteckert, Phys. Rev. Lett. **101**, 140601 (2008).
[43]L. Borda and A. Zawadowski, Phys. Rev. B **81**, 153303 (2010).
[44]Even though the chain has $N + 1$ bath sites, we refer to it either as an N-site chain or a chain of length N, so as to emphasize the number of distinct hopping matrix elements or energy scales involved.
[45]E. Lebanon, A. Schiller, and F. B. Anders, Phys. Rev. B **68**, 155301 (2003).
[46]S. R. White, Phys. Rev. Lett. **69**, 2863 (1992); Phys. Rev. B **48**, 10345 (1993).
[47]E. R. Davidson, J. Comput. Phys. **17**, 87 (1975).
[48]A. Greilich, A. Shabaev, D. R. Yakovlev, A. L. Efros, I. A. Yugova, D. Reuter, A. D. Wieck, and M. Bayer, Science **317**, 1896 (2007).
[49]For a hybrid chain, one can no longer use the NRG to generate the ground state of $\mathcal{H}^a$. In this case, one can use the Davidson method [47] to construct the initial state, as discussed in Sec. II C 3.
[50]M. Yoshida, M. A. Whitaker, and L. N. Oliveira, Phys. Rev. B **41**, 9403 (1990).
[51]P. Schlottmann, Phys. Rev. B **25**, 4815 (1982).
[52]M. Heyl and S. Kehrein, Phys. Rev. B **81**, 144301 (2010).